Mixing Variability in the Southern Ocean

AMELIE MEYER

CSIRO Ocean and Atmosphere Flagship, and Institute for Marine and Antarctic Studies, University of Tasmania, Hobart, Australia

BERNADETTE M. SLOYAN

CSIRO Ocean and Atmosphere Flagship, Hobart, Australia

KURT L. POLZIN

Woods Hole Oceanographic Institution, Woods Hole, Massachusetts

HELEN E. PHILLIPS

Institute for Marine and Antarctic Studies, University of Tasmania, and ARC Centre of Excellence for Climate System Science, Hobart, Australia

NATHANIEL L. BINDOFF

CSIRO Ocean and Atmosphere Flagship, and ARC Centre of Excellence for Climate System Science, and Institute for Marine and Antarctic Studies, University of Tasmania, and Antarctic Climate and Ecosystems CRC, Hobart, Australia

(Manuscript received 6 June 2014, in final form 18 December 2014)

ABSTRACT

A key remaining challenge in oceanography is the understanding and parameterization of small-scale mixing. Evidence suggests that topographic features play a significant role in enhancing mixing in the Southern Ocean. This study uses 914 high-resolution hydrographic profiles from novel EM-APEX profiling floats to investigate turbulent mixing north of the Kerguelen Plateau, a major topographic feature in the Southern Ocean. A shear–strain finescale parameterization is applied to estimate diapycnal diffusivity in the upper 1600 m of the ocean. The indirect estimates of mixing match direct microstructure profiler observations made simultaneously. It is found that mixing intensities have strong spatial and temporal variability, ranging from $O(10^{-6})$ to $O(10^{-3})$ $m^2\,s^{-1}$. This study identifies topographic roughness, current speed, and wind speed as the main factors controlling mixing intensity. Additionally, the authors find strong regional variability in mixing dynamics and enhanced mixing in the Antarctic Circumpolar Current frontal region. This enhanced mixing is attributed to dissipating internal waves generated by the interaction of the Antarctic Circumpolar Current and the topography of the Kerguelen Plateau. Extending the mixing observations from the Kerguelen region to the entire Southern Ocean, this study infers a large water mass transformation rate of 17 Sverdrups (Sv; 1 Sv $\equiv 10^6\,m^3\,s^{-1}$) across the boundary of Antarctic Intermediate Water and Upper Circumpolar Deep Water in the Antarctic Circumpolar Current. This work suggests that the contribution of mixing to the Southern Ocean overturning circulation budget is particularly significant in fronts.

1. Introduction

In the stratified ocean, turbulent mixing is primarily attributed to the dissipation of internal waves. Recent work suggests that in some regions of the Southern Ocean, the interaction between the Antarctic Circumpolar Current, or tidal flows, and rough topography is a significant source of internal waves (e.g., Naveira Garabato et al. 2004b; Nikurashin and Ferrari 2010). There is growing evidence that the resulting enhanced mixing over regions of rough topography affects the abyssal stratification, the circulation of the Southern

Corresponding author address: Amelie Meyer, Norwegian Polar Institute, Framsenteret, 9296 Tromsø, Norway.
E-mail: amelie.meyer@npolar.no

DOI: 10.1175/JPO-D-14-0110.1

Ocean, and the global overturning circulation (Naveira Garabato et al. 2004b; Sloyan et al. 2010; Nikurashin and Ferrari 2010). This work investigates small-scale diapycnal turbulent mixing and its sources north of the Kerguelen Plateau, a major topographic feature in the Southern Ocean.

Understanding the processes affecting small-scale mixing in the oceans and how they can be parameterized in circulation models is still a challenge in physical oceanography (Alford et al. 2012). In spite of much work on new instruments and techniques to measure turbulence, observations of mixing are sparse and our limited understanding of the physical processes behind turbulent mixing leads to inaccurate representations of mixing in ocean general circulation models (Wunsch and Ferrari 2004). High-resolution modeling studies have shown that the uptake and storage of tracers, such as heat, salt, nutrients, and gases, are very sensitive to the temporal and spatial variations of mixing (Harrison and Hallberg 2008). With turbulent mixing playing a key role in the overturning circulation and in the budgets of energy, carbon, and nutrients, it is crucial to have a correct representation of mixing in ocean models (Gregg et al. 2003).

Turbulent mixing leads to the transfer of kinetic energy into heat by viscous dissipation. The heat generated by turbulence is typically insignificant compared to that of other sources such as solar radiation (Thorpe 2005), but the total loss of energy by turbulent motions is substantial and must be balanced by other energy sources for the ocean to remain in a quasi-steady state. As such, turbulent mixing can control the strength of the ocean's overturning circulation (Bryan 1987), dissipating energy from the winds and tides. The eddy diffusion coefficient of mass across isopycnal surfaces, called diapycnal turbulent eddy diffusivity of mass and hereinafter referred to as diffusivity (K_ρ), is often used to characterize turbulent mixing.

The Southern Ocean has no meridional continental barriers. This allows for the existence of the eastward-flowing Antarctic Circumpolar Current that connects the three major ocean basins and is composed of intense narrow fronts (Deacon 1937). These fronts coincide with water mass boundaries and maxima in current speed (Orsi et al. 1995). Eddies with length scales ranging from tens to hundreds of kilometers are found along the path of the Antarctic Circumpolar Current. These eddies carry heat poleward and are key to Southern Ocean dynamics (Olbers et al. 2004). The Southern Ocean meridional circulation is driven by winds and surface buoyancy forcing (Rintoul and Naveira Garabato 2013). It consists of the upwelling of deep waters to the surface and the production of dense bottom and intermediate waters. The Southern Ocean therefore regulates fluxes of heat, freshwater, and carbon between the surface and the deep ocean (Rintoul and Naveira Garabato 2013). Dense waters are formed in a few regions at high latitudes and mass balance requires the conversion of these waters to less dense water masses. This can be achieved through diapycnal mixing where the downward diffusion of heat is balanced by the upward diapycnal advection of the overturning circulation (Munk 1966). Recent work suggests that the conversion of dense waters to less dense waters can be buoyancy and wind driven in the Southern Ocean, where abyssal isopycnals outcrop at the surface (Toggweiler and Samuels 1995, 1998; Nikurashin and Vallis 2012). The quantitative contribution of either diapycnal mixing or buoyancy fluxes is unknown, but diapycnal mixing at least partly closes the Southern Ocean meridional circulation by upwelling tracers across isopycnals (Huang 1999). As such, the intensity and distribution of diapycnal mixing in the Southern Ocean plays a major role in the global overturning circulation (Polzin et al. 1997; Sloyan and Rintoul 2001; Wunsch and Ferrari 2004; Ferrari 2014).

Both the wind, through wind work at the ocean surface (Wunsch 1998) and through variations in the wind forcing (Alford 2001; Watanabe and Hibiya 2002), and the buoyancy gradient are sources of energy for the global ocean circulation. One sink for this energy is turbulent mixing. Assuming uniform mixing, Munk (1966) used an advective and diffusive model of heat transfer to estimate that $K_\rho = 10^{-4}\,\mathrm{m^2\,s^{-1}}$ was required to close the global meridional overturning circulation. The relationship $K_\rho = 10^{-4}\,\mathrm{m^2\,s^{-1}}$ became the canonical value for diffusivity throughout the ocean interior. Observations of diffusivity in the thermocline waters determined by tracer release (Ledwell et al. 1993, 1998), and microstructure studies (Gregg 1987), sparked controversy with values of diffusivity an order of magnitude lower than the canonical value. For the past 20 yr, observational estimates have shown diffusivity to be highly spatially nonuniform, with values above rough topography up to two orders of magnitude larger than the canonical value (Polzin et al. 1996, 1997; Ledwell et al. 2000; St. Laurent et al. 2001; Naveira Garabato et al. 2004b; Sloyan 2005). A recent compilation of global values of observed mixing shows mean diffusivities are $O(10^{-4})\,\mathrm{m^2\,s^{-1}}$ below 1000-m depth and $O(10^{-5})\,\mathrm{m^2\,s^{-1}}$ above (Waterhouse et al. 2014). These estimates well match the Munk canonical value and point to the spatial variability in intensity, generation, and dissipation of mixing. Such observations question the assumption of uniform turbulent mixing. The significance of topography is of particular importance in the Southern Ocean since the stratification is weak compared to the global ocean and since the Antarctic Circumpolar Current is

quasi barotropic with strong currents extending to the seafloor.

We are left with the following questions: 1) Are there enough turbulent mixing hot spots ($K_\rho > 10^{-4}\,\mathrm{m^2\,s^{-1}}$) in the ocean to account for the globally averaged diffusivity ($K_\rho \approx 10^{-4}\,\mathrm{m^2\,s^{-1}}$) required to close the meridional overturning circulation? 2) What is the relative contribution of eddy–mean flow interaction and flow–topography interaction to Southern Ocean dynamics? 3) How do regional dynamics influence the magnitude and variability of mixing? 4) Is it the tides, large mesoscale eddies, fronts, or a combination of all that interact with the rough topography to generate internal waves? This paper contributes primarily to questions 2 and 3 and, to a lesser extent, questions 1 and 4.

We present the first estimates of turbulent mixing from Electromagnetic Autonomous Profiling Explorer (EM-APEX) floats. Our key finding is that the high mixing variability observed near the Kerguelen Plateau can be attributed to regional dynamics. We infer mixing sources and identify regional dynamics by analyzing the influence of environmental factors on the mixing distribution. The data and quality control applied are described in section 2. In section 3, we present the method of finescale parameterization of shear and strain to estimate turbulent mixing. Aspects of the regional oceanography, mixing levels, sources, and regional dynamics are described in section 4. In section 5, we discuss the implications in a regional context.

2. Data

Observations

The observations for this study were collected in late 2008 north of the Kerguelen Plateau as part of the Southern Ocean Finestructure (SOFine) project. SOFine is a United Kingdom, United States, and Australian collaborative project to investigate the impact of finescale processes on the momentum balance in the Antarctic Circumpolar Current (Naveira Garabato 2009). The SOFine oceanographic survey consisted of 59 sampling stations, a mooring array, and eight EM-APEX Argo-equivalent floats deployed along the ship track. At the stations, simultaneous measurements of conductivity–temperature–depth (CTD), lowered acoustic Doppler current profiler (LADCP), and free-falling vertical microstructure profiler (VMP) were made (Waterman et al. 2013). A moored array was deployed on a ridge that extends northward from the Kerguelen Plateau between 46.50° and 47.00°S and 71.75° and 72.00°E. Three moorings were short term, while two other moorings were deployed for 2 yr (Naveira Garabato 2009). In this study, we use the data from the EM-APEX floats to understand the variability of mixing in the region. The EM-APEX floats were deployed on the northern edge of the Kerguelen Plateau. Programed to surface twice a day, they were advected eastward by the Antarctic Circumpolar Current. We use a subset of 914 profiles of temperature, salinity, pressure, and horizontal velocity from the ocean surface to 1600-m depth sampled over a period of 10 weeks in the vicinity of the Kerguelen Plateau. The profiles that the floats sampled downstream from the Kerguelen Plateau are not examined.

The EM-APEX profiling float is an innovative instrument that provides inexpensive, autonomous, and high-resolution observations of horizontal velocity. It combines a standard Teledyne Webb Autonomous Profiling Explorer float with a velocity-sensing electromagnetic subsystem. A Sea-Bird Electronics SBE-41 CTD instrument measures the temperature, salinity, and pressure. The CTD is pumped on demand for approximately 2.5 s, delivering $40\,\mathrm{ml\,s^{-1}}$ flow. The EM-APEX electromagnetic subsystem has a compass, accelerometer, and five electrodes to estimate the magnitude of the horizontal velocity. The principle is that a conductor moving through a magnetic field develops an electrical potential drop across the conductor; the conductor is seawater, and the magnetic field is that of Earth (Sanford et al. 1978). The EM-APEX electromagnetic subsystem voltmeter measures the electric potential difference across the body of the float with two independent pairs of electrodes. The processing of the voltages into velocity components is shore based. The EM-APEX float rate of ascent and descent ranges from 0.12 to $0.13\,\mathrm{m\,s^{-1}}$, resulting in velocity estimates at approximately 3-m vertical intervals.

The temperature, salinity, and pressure data from the EM-APEX floats were quality controlled by adapting and applying the CSIRO Marine and Atmospheric Research Argo delayed-mode quality control procedure (Meyer et al. 2015, unpublished manuscript). This was followed by processing to calibrate the relative velocities measured by the floats and combine them with GPS surface positions to produce absolute velocity profiles (Phillips and Bindoff 2014).

3. Shear–strain parameterization of the turbulent dissipation rate

Turbulence is strongly related to the energy and shear of the internal wave field through wave–wave interactions (Polzin et al. 1995). The local turbulent dissipation rate can be estimated by combining observations of the internal wave field (finescale measurements) with theoretical models of energy transfer. Finescale parameterizations have been widely used to estimate mixing in the past

decade (e.g., Mauritzen et al. 2002; Naveira Garabato et al. 2004b; Sloyan 2005; Kunze et al. 2006; Alford et al. 2007; Park et al. 2008; Fer et al. 2010; Wu et al. 2011; Whalen et al. 2012; MacKinnon et al. 2013). The use of finescale parameterization is high since the observations needed (vertical density and/or velocity measurements) to derive the dissipation rate with these methods are more easily acquired than direct observations of dissipation using microstructure profilers.

The finescale parameterization is based on 1) the assumption that most of the turbulent mixing is driven by breaking internal waves (Alford and Gregg 2001) and 2) the notion of a downscale energy cascade. Garrett and Munk (hereinafter GM) were the first to describe and model the background internal wave field empirically in terms of a vertical wavenumber and frequency spectrum (Garrett and Munk 1972). Additional work by Garrett and Munk (1975) and modifications by Cairns and Williams (1976), denoted GM75 and GM76, respectively, further characterized the background internal wave field. Gregg (1989) then applied models to shear observations to obtain estimates of the dissipation rate. Over the next 20 yr, theoretical work (e.g., Lvov et al. 2004), observational work (e.g., Polzin et al. 1995), and numerical simulations (e.g., Winters and D'Asaro 1997) further tested and refined the model of energy transfer. It predicts the turbulent dissipation rate from the energy level of internal waves as derived from finescale measurements of the vertical shear (from velocity profiles) and vertical strain (from density profiles).

As suggested by the theory (Henyey et al. 1986) and observations (Polzin et al. 1995), the dissipation rate scales quadratically with the shear spectral level. Assuming the spectral energy transfer arrives at dissipation scales where wave-breaking dissipates turbulent kinetic energy, the dissipation rate ε is

$$\varepsilon = \varepsilon_0 \left(\frac{N^2}{N_0^2}\right) \frac{\langle V_z^2\rangle^2}{\langle V_{z-\mathrm{GM}}^2\rangle^2} \frac{3(R_\omega+1)}{2\sqrt{2}R_\omega(R_\omega-1)^{1/2}} \frac{f\cosh^{-1}(N/f)}{f_0\cosh^{-1}(N_0/f_0)}. \quad (1)$$

We follow the Polzin et al. (2002) and Naveira Garabato et al. (2004a) notations where N is the "local" buoyancy frequency, $\langle V_z^2\rangle$ is the integrated variance of the vertical shear normalized by N, $\langle V_{z-\mathrm{GM}}^2\rangle$ is the GM76 model-integrated vertical shear variance, R_ω is the shear-to-strain variance ratio, and f is the local inertial frequency. Equation (1) is normalized to the GM76 model (latitude 32.5°N) such that constants are the dissipation $\varepsilon_0 = 8 \times 10^{-10}\,\mathrm{W\,kg^{-1}}$, the buoyancy frequency $N_0 =$ 3 cph extrapolated to the surface in GM76, and the inertial frequency $f_0 = 7.86 \times 10^{-5}\,\mathrm{s^{-1}}$. Here, the angle brackets denote variance integrated over a specified vertical wavenumber range. For further details, Polzin et al. (2014) provide an in-depth discussion on how to estimate turbulent dissipation with finescale parameterizations.

The buoyancy frequency N is expressed as an angular frequency in radians per second:

$$N = \sqrt{gE} \simeq \sqrt{-\frac{g}{\rho_\theta}\frac{d\rho_\theta}{dz}}, \quad (2)$$

where g is the acceleration due to gravity, E is the stability of the water column, and ρ_θ is the potential density. To estimate the buoyancy frequency from the EM-APEX data, we use a potential density derived at local reference levels through the water column. We apply the adiabatic steric anomaly levelling method developed by Bray and Fofonoff (1981) where the potential density gradient is estimated using a linear regression after levelling to a midpoint reference pressure. For the purpose of this study, we estimate two buoyancy frequencies that are derived over different time, horizontal, and vertical length scales. First, we derive the squared buoyancy frequency N^2. For this small-scale N^2, the density gradient is estimated using a linear regression of potential density on pressure, calculated over a vertical pressure window of 12 m in Eq. (2). We use the same method to derive the mean squared buoyancy frequency $\langle N_{\mathrm{ref}}^2\rangle$, using a longer vertical averaging pressure window (24 m) as well as a horizontal averaging window. The brackets $\langle\ \rangle$ denote horizontal averaging over 20 profiles. Strain (ξ_z) is derived as $\xi_z = (N^2 - \langle N_{\mathrm{ref}}^2\rangle)/\langle N_{\mathrm{ref}}^2\rangle$, where N^2 is the squared buoyancy frequency, and $\langle N_{\mathrm{ref}}^2\rangle$ is the mean squared buoyancy frequency.

We spatially Fourier transform each strain ξ_z and shear V_z segment to obtain the strain spectra Φ_{strain} and the shear spectra Φ_{shear}, respectively. The shear variance $\langle V_z^2\rangle$ and the strain variance $\langle \xi_z^2\rangle$ are then determined by integrating the shear spectra and the strain spectra from a minimum vertical wavenumber m_0 to a cutoff vertical wavenumber m_c [Eq. (3)]. Ideally, this window covers the entire internal wave band, particularly if the spectra are not flat. It can be set to a constant range such as 50 to 300 $\mathrm{cpm^{-1}}$ (Damerell et al. 2012) to a variable range (Naveira Garabato et al. 2004b; Whalen et al. 2012; Waterman et al. 2013), but this window rarely integrates to the cutoff vertical wavenumber. The cutoff vertical wavenumber m_c is the threshold where there is a transition from quasi-linear wave–wave interactions to strongly nonlinear wave breaking (D'Asaro and Lien 2000). Here, the high vertical resolution of the velocity data from the EM-APEX floats (~3 m) enables us to resolve the appropriate cutoff vertical wavenumber for each profile. We define the cutoff vertical wavenumber as the point where the integrated shear variance reaches

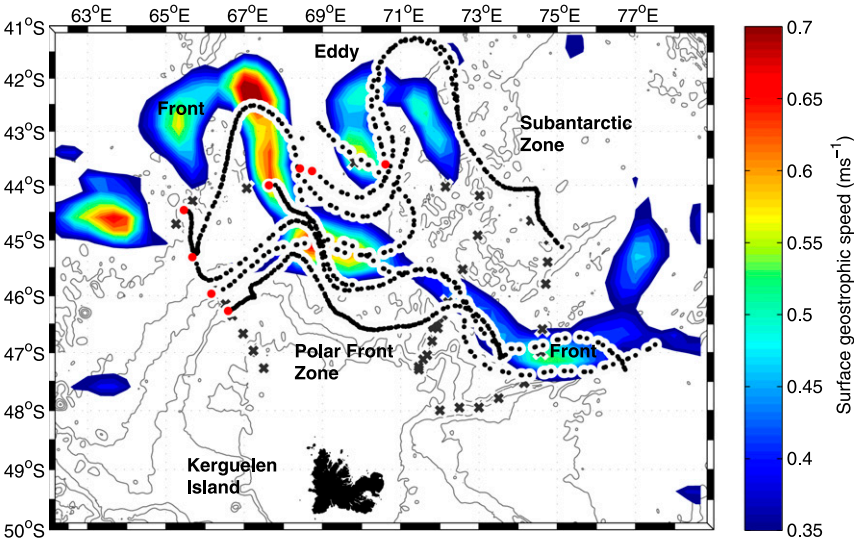

FIG. 1. EM-APEX float trajectories overlying topography contours (gray) ranging from 500 to 5000 m at 800-m increments. Each black dot denotes the surface location of a float profile and the deployment location is highlighted with a red dot. Gray crosses indicate the location of available microstructure profiler data from the SOFine cruise. To identify frontal jets, we show the mean surface geostrophic speed over 0.35 m s^{-1} during the sampling period (color scale).

$2\pi N^2/10$ and derive it for each vertical segment. Its mean value is 16 cpm^{-1}. We then set the minimum vertical wavenumber to $m_0 = 384\,cpm^{-1}$, a compromise between integrating at wavenumbers low enough to resolve vertical structure but not so low that nonwave (e.g., geostrophically balanced motion) variance contaminates the spectra:

$$\langle V_z^2\rangle = \int_{m_0}^{m_c} \Phi_{\text{shear}}\, dk \quad \langle \xi_z^2\rangle = \int_{m_0}^{m_c} \Phi_{\text{strain}}\, dm. \qquad (3)$$

The shear variance from the GM76 model spectrum $\langle V_{z-\text{GM}}^2\rangle$ [Eq. (1)] is derived from integrating over the same wavenumber band (m_0 to m_c), using the GM model parameters from GM76.

The shear-to-strain variance ratio R_ω is

$$R_\omega = \frac{\langle V_z^2\rangle}{\langle \xi_z^2\rangle} \qquad (4)$$

and is derived for each vertical segment of each profile. It is an estimate of the mean aspect ratio of the internal wave field from which a measure of the bulk frequency of the wave field content can be derived (Polzin et al. 2014). Higher R_ω values imply a dominant presence of near-inertial waves, while lower R_ω values can be attributed to the presence of more high-frequency internal waves at high vertical wavenumber or the presence of shear instabilities when $m > m_c$ (Polzin et al. 2003).The shear-to-strain variance ratio is also used in strain-only finescale parameterizations to estimate mixing, where the choice of R_ω is based on observed R_ω from previous studies.

To estimate the diapycnal turbulent eddy diffusivity K_ρ from the dissipation rate ε, we use the Osborne and Burch (1980) relation

$$K_\rho = \Gamma \frac{\varepsilon}{N^2}, \qquad (5)$$

where the mixing efficiency ($\Gamma = 0.2$) is assumed to be a constant (Osborne and Burch 1980). The uncertainty associated with deriving the dissipation rate and the diapycnal turbulent eddy diffusivity is estimated as a factor of ±2 (Polzin et al. 1995). The software we developed to estimate mixing from EM-APEX data is described in Meyer et al. (2014) and is available online.[1]

4. Results

a. Regional oceanography

The profiles from the EM-APEX floats stretch over 6500 km of float trajectories in the vicinity of the Kerguelen Plateau (41°–50°S, 61°–79°E), sampling the upper water column (0 to 1600 m) between November 2008 and January 2009 (Fig. 1). The profiles of potential

[1] http://au.mathworks.com/matlabcentral/fileexchange/47595-mixing–mx–oceanographic-toolbox-for-em-apex-float-data

temperature, salinity, horizontal velocity, and buoyancy frequency from the EM-APEX floats help us identify oceanographic features near the Kerguelen Plateau (Fig. 2). In Figs. 2 and 3a, profiles are shown in sampling order and are grouped by floats. The floats are organized by each float's mean latitude from south to north. This gives to the composite trajectories the appearance of a meridional transect with the southernmost float on the left-hand side (Figs. 2, 3a).

Fronts can be identified using hydrographic criteria such as velocity maxima location, water mass distribution, and locations where certain hydrographic properties cross particular depths (Belkin and Gordon 1996). Traditionally, the Subtropical Front is identified by a temperature range of 10° to 12°C and salinities on the practical salinity scale (pss-78) of 34.6 to 35.0 at 100-m depth (Orsi et al. 1995). The Subantarctic Front is located at the rapid descent of the subsurface salinity minimum (Whitworth and Nowlin 1987), and the Polar Front can be defined by the northern limit of the subsurface 2°C temperature minimum at the 200- to 300-m depth range (Park et al. 1998). Recent studies have shown that fronts in the Antarctic Circumpolar Current are complex and that their position and intensity are highly variable in time (Sokolov and Rintoul 2007, 2009). Upstream and downstream from topographic features, fronts have many branches that merge, diverge, and meander with time. The different branches of the Subantarctic Front are known to merge into an intense jet north of the Kerguelen Plateau, while downstream of the plateau, the jet shows a strong variability and the fronts split (Sallée et al. 2008). The location of the Polar Front in the region of the Kerguelen Plateau is variable. The northern branch of the Polar Front has been observed (Belkin and Gordon 1996) and modeled (Langlais et al. 2011) to pass both north and south (Park et al. 1998) of the Kerguelen Plateau with the possibility of atmospheric forcing as a control factor (Sallée et al. 2008).

We use surface velocity maxima determined from satGEM (Meijers et al. 2011), a weekly geostrophic velocity product, as an indication of the position of fronts. SatGEM combines a gravest empirical mode (GEM) analysis of ocean climatology data and satellite altimetry data (AVISO). We average the weekly satGEM geostrophic velocities over the sampling period of the EM-APEX floats (18 November 2008–30 January 2009) and over a density range of 26.6 to 26.8 $\mathrm{kg\,m^{-3}}$. The result is a mean surface geostrophic velocity field with a horizontal resolution of 1/3°, in which we find a coherent and intense jet north of the Kerguelen Plateau (Fig. 1). This jet diverges and splits at 80°E, downstream of the Kerguelen Plateau. We identify this jet as the middle and northern branches of the Subantarctic Front, likely merged with the southern branch of the Subtropical Front. Float 3762 crossed the path of this jet at 42.5°S, 67.5°E, recording a jump from south to north in temperature from 5.21° to 11.36°C and in salinity from 34.05 to 34.85 at 200-m depth, which corresponds to both the ranges of the Subantarctic Front and Subtropical Front (Figs. 2a,b). We refer to this front as the Subantarctic/Subtropical Front (SAF/STF). Damerell et al. (2013) defined a similar front using the SOFine ship-based hydrographic data from the same region and same time period. The EM-APEX floats do not sample the Polar Front. There is no jet signature between the SAF/STF region and Kerguelen Island to indicate the Polar Front position. More significantly, there is no 2°C isotherm in the 100- to 300-m depth range in the EM-APEX profiles. Only the 2.2°C isotherm appears at 300 m in the first 50 profiles of the southernmost float (float 3760).

A feature observed in both the EM-APEX data and the satGEM product is a large meanderlike structure pinching off the SAF/STF region, hereinafter called the eddy (Fig. 1). We confirm this feature is a cold-core cyclonic eddy located between 44° and 42°S and 69° and 73°E using satellite sea surface temperature data (not shown). Three EM-APEX floats (floats 4051, 3764, and 3951) sampled along the rim of the eddy but did not sample its core. The eddy rim has the same temperature, salinity, and density characteristics as surrounding waters; however, its current speed is higher than surrounding waters. In the top 200 m of the eddy rim, the stratification is low compared to either the SAF/STF region or the Subantarctic zone (Fig. 2d; profiles 720 to 800).

We sort the EM-APEX float profiles according to their position relative to the fronts. They are either in the region north of the SAF/STF region (Subantarctic zone), in the SAF/STF region, in the region south of the SAF/STF region (Polar Front zone), or in the eddy. Profiles located in a region of geostrophic flow velocity larger than 0.35 $\mathrm{m\,s^{-1}}$ are considered to be in the SAF/STF region or in the eddy if not along the main axis of the SAF/STF region. The rest of the profiles are assigned to either the Subantarctic zone or to the Polar Front zone. Half the profiles are found to be in the Polar Front zone, 23% in the SAF/STF region, 10% in the Subantarctic zone, and 16% in the eddy.

South of the SAF/STF region, we identify Upper Circumpolar Deep Water (UCDW) as the water mass with potential density $\sigma_\theta \geq 27.5\,\mathrm{kg\,m^{-3}}$ (Fig. 2). This corresponds to water cooler than 2.34°C and salinity above 34.5. North of the SAF/STF, we define Subantarctic Mode Water (SAMW) as $\sigma_\theta \leq 27.1\,\mathrm{kg\,m^{-3}}$ and the Antarctic Intermediate Water (AAIW) as $27.1 \leq \sigma_\theta \leq 27.5\,\mathrm{kg\,m^{-3}}$, which corresponds to potential temperature $2.7°\mathrm{C} \leq \theta \leq 5.8°\mathrm{C}$ and salinity $34.4 \leq S \leq 34.7$. These definitions are consistent with those used by Sloyan and Rintoul (2001) and Damerell et al. (2013).

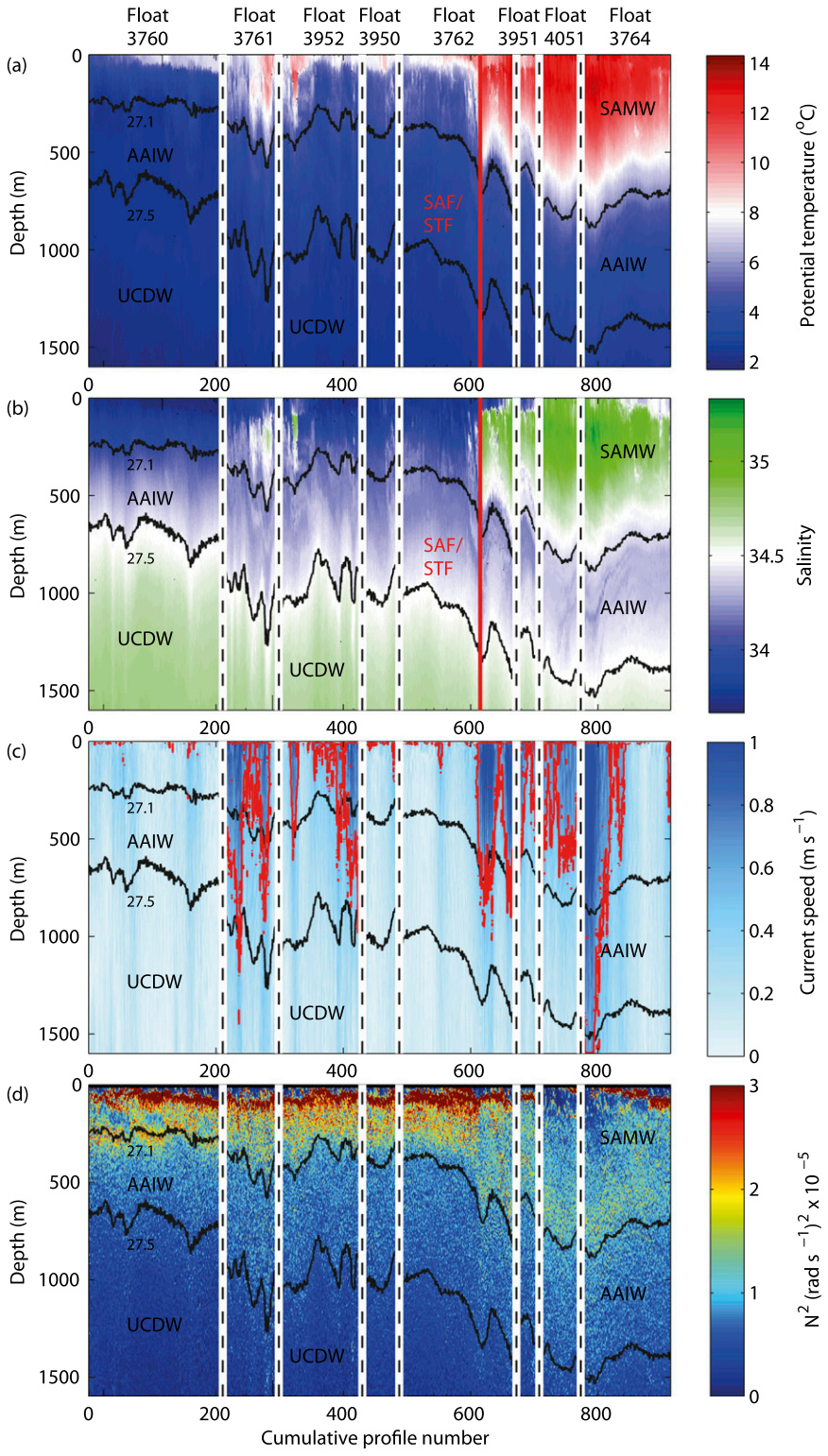

FIG. 2. Vertical distribution of (a) potential temperature, (b) salinity, (c) current speed, and (d) buoyancy frequency squared (N^2) along the trajectories of the eight EM-APEX floats. The position of the SAF/STF region is indicated by the vertical red line in (a) and (b). Selected labeled potential density (σ_θ) contours delimit water masses north and south of the SAF/STF region. Water masses are defined as $\sigma_\theta \leq 27.1\,\mathrm{kg\,m^{-3}}$ for SAMW, $27.1 \leq \sigma_\theta \leq 27.5\,\mathrm{kg\,m^{-3}}$ for AAIW, and $\sigma_\theta \geq 27.5\,\mathrm{kg\,m^{-3}}$ for UCDW. (c) The $0.55\,\mathrm{m\,s^{-1}}$ current speed contour (red) identifies the location of jets. Vertical dashed lines separate floats.

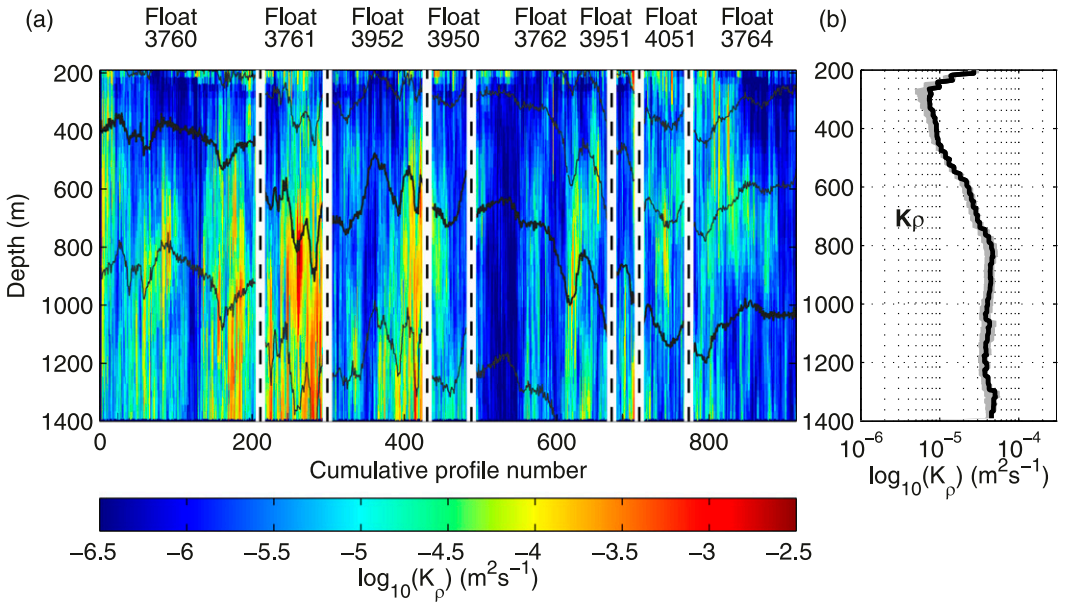

FIG. 3. (a) Vertical distribution of diffusivity (K_ρ) along the trajectories of the eight EM-APEX floats. Potential density contours (σ_θ = 26.7, 27.0, 27.3 (thick), and 27.6 kg m^{-3}) are shown by the black lines. The vertical dashed lines separate floats. (b) Mean vertical profile of diffusivity (K_ρ) estimated using the shear–strain parameterization from the EM-APEX data. Shaded areas show the 90% confidence intervals computed via standard deviation with bootstrap sampling.

b. *Intensity and spatial distribution of mixing*

Values of diffusivity K_ρ estimated from the EM-APEX data with the shear–strain parameterization show large variability (Fig. 3a) and vary by as much as four orders of magnitude in one profile. Some regions (approximately profiles 500 to 560 and 880 to 914) show particularly weak diffusivities of $O(10^{-6})$ m^2 s^{-1}. Other regions show enhanced diffusivity values of $O(10^{-3})$ m^2 s^{-1} below 600 m in the vicinity of rough topography (approximately profiles 170, 290, and 420) and of $O(10^{-4})$ m^2 s^{-1} (approximately profiles 700 to 840) in the upper 200 m (Fig. 3a).

The overall mean diffusivity is 3×10^{-5} m^2 s^{-1}with a 90% confidence interval of 2.5×10^{-5} to 3.4×10^{-5} m^2 s^{-1} (Fig. 3b). The mean dissipation rate ε is 9×10^{-10} W kg^{-1} with a 90% confidence interval of 7.0×10^{-10} to 9.7×10^{-10} W kg^{-1}. It is often assumed that the dissipation rate in the open ocean at mid- and low latitudes is $O(10^{-10})$ W kg^{-1} (St. Laurent et al. 2012), placing our mean dissipation rate at background levels. However, we find that vertically averaged dissipation is highly spatially variable and most intense over shallower bathymetry and rough topography (Fig. 4). In particular, EM-APEX floats close and downstream from the Kerguelen Plateau (floats 3761, 3760, and 3952) show high vertically averaged dissipation. The mixing estimates are similar to other finescale parameterization observations in the Southern Ocean (Wu et al. 2011) and microstructure measurements north of the Kerguelen Plateau (Waterman et al. 2013).

c. *Environmental factors and mixing variability*

Here, we investigate topographic roughness, current speed, and wind speed as environmental factors controlling the variability of the mixing.

1) TOPOGRAPHY

For each EM-APEX float profile, we derive the topographic roughness as the variance of bottom height H [var(H)] in square meters. The topographic roughness is computed over a 0.1° longitude by 0.1° latitude box, which is approximately 8 km × 11 km, using the topography dataset from Smith and Sandwell, version 13.1 (Smith and Sandwell 1997).[2] The spatial resolution of the topography dataset resolves only part of the scales of the internal lee-wave generation radiative range (Nikurashin and Ferrari 2011). Beside the Smith and Sandwell topographic dataset, methods exist to estimate regional small-scale topographic roughness (Nikurashin and Ferrari 2011). However, such methods require adding a parametric spectral component by Goff and Jordan (1988) to the measured topographic spectrum. Here, we choose to use the Smith and Sandwell topography data.

[2] http://topex.ucsd.edu/WWW_html/mar_topo.html

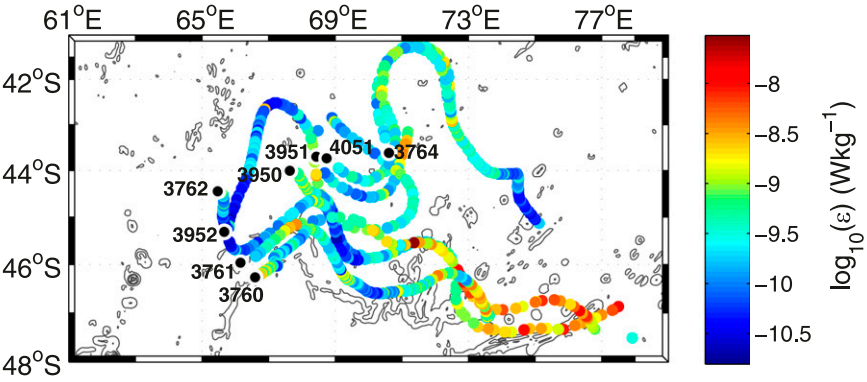

FIG. 4. Horizontal distribution of vertically averaged (200 to 1400 m) dissipation ε from shear–strain parameterization. Topographic roughness contours range from the mean roughness of the area ($1.72 \times 10^{-4}\,m^2$) to $50 \times 10^{-4}\,m^2$ at $15 \times 10^{-4}\,m^2$ intervals (gray). Float numbers are indicated as well as the first profile of each float (black dot).

We subsample the mixing data into profiles above smooth topography and profiles above rough topography. Smooth topography is defined as values of roughness less than the mean, $1.72 \times 10^4\,m^2$, and rough topography as values of roughness larger than the mean. Most profiles sampled above rough topography are located south of 45°S closer to the Kerguelen Plateau. The mean vertical mixing profiles show that dissipation is up to 3 times more intense above rough topography than above smooth topography (Fig. 5), while the mean vertical stratification and horizontal velocity profiles are similar whether above smooth or rough topography (not shown). The mean profile above rough topography shows enhanced dissipation from 240 to 1400 m, with a maximum near 800 m. The water column above rough topography is on average 2900 m deep in this study. This suggests that the impact of the topography on mixing in this case might reach up to 2000 m above the seafloor, as previously reported in the Brazil basin (Polzin et al. 1997).

Additionally, we observe a significant correlation of $R = 0.74$ ($P < 0.05$ at the 95% confidence interval) between the topographic roughness and depth-integrated diffusivity over the total profile range (not shown). The linear fit between the topographic roughness and the diffusivity has a slope of 0.58. The correlation $R = 0.74$ north of the Kerguelen Plateau is higher than previously estimated for the whole Southern Ocean ($R = 0.51$ at the 95% confidence interval; Wu et al. 2011).

2) CURRENT SPEED

To quantify the impact of the SAF/STF region on the mixing intensity, we estimate the correlation between the depth-integrated diffusivity (800–1400 m) and the mean current speed in the upper 1400 m, assuming that higher mean current speed is a good proxy for the frontal region. Over the whole dataset, the moderate positive correlation ($R = 0.36$ and $P < 0.05$ at the 95% confidence interval) confirms that as current speed increases, so does mixing. The enhanced mixing associated with high current speed is likely because of the internal wave generation and dissipation where the strong quasi-steady flow of the Antarctic Circumpolar Current interacts with the topography (Bell 1975). Such enhanced mixing would be located closer to the seafloor where the internal waves dissipate. We therefore expect a stronger correlation in profiles in shallower water, where the floats sample a larger percentage of the water column. We choose the mean water depth (3546 m) over 41°–50°S and 61°–79°E as a threshold value, and we correlate current speed and depth-integrated diffusivity only for profiles in less than 3546 m (Fig. 6). The resulting correlation is stronger $R = 0.63$ ($P < 0.0005$ at the 95% confidence interval), confirming the presence of enhanced mixing at depth when the current speed is high.

High current speed can be the result of geostrophic flows and tidal flows. We investigate how much, if any, of the enhanced mixing at depth could be the result of tidal motions rather than geostrophic motions. A detailed analysis of recent estimates of the energy conversion from M_2 barotropic tide (Egbert and Ray 2000) and geostrophic motions (Nikurashin and Ferrari 2013) into internal waves shows that geostrophic motions dominate energy conversion into internal waves near the Kerguelen Plateau and that tidal energy dissipation is only significant on the edge and above the Kerguelen Plateau (not shown). A harmonic analysis of the data from the SOFine long-term moorings close to the plateau shows that the mean tide (including M_2, S_2, N_2, K_1, O_1, and P_1) for the full water column is $2.31\,cm\,s^{-1}$ with a range of 0.02 to $5.89\,cm\,s^{-1}$, while below 1500 m, the mean tide is $1.17\,cm\,s^{-1}$ with a range of 0.01 to $3.6\,cm\,s^{-1}$. These estimates are far smaller than the

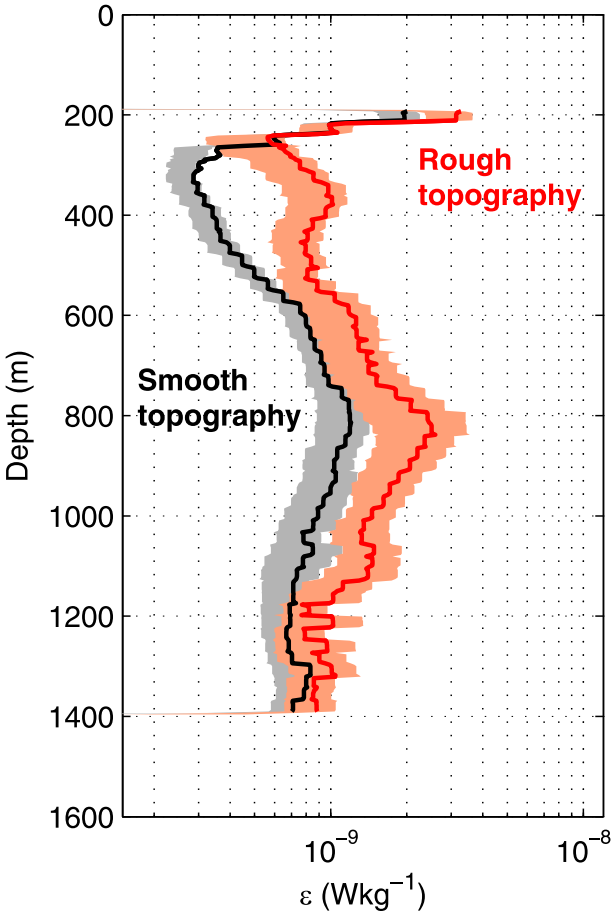

FIG. 5. Mean vertical dissipation ε profile as a function of depth above rough topography (red) and smooth topography (black). Shaded areas show the 90% confidence intervals computed as the standard deviation from bootstrap sampling.

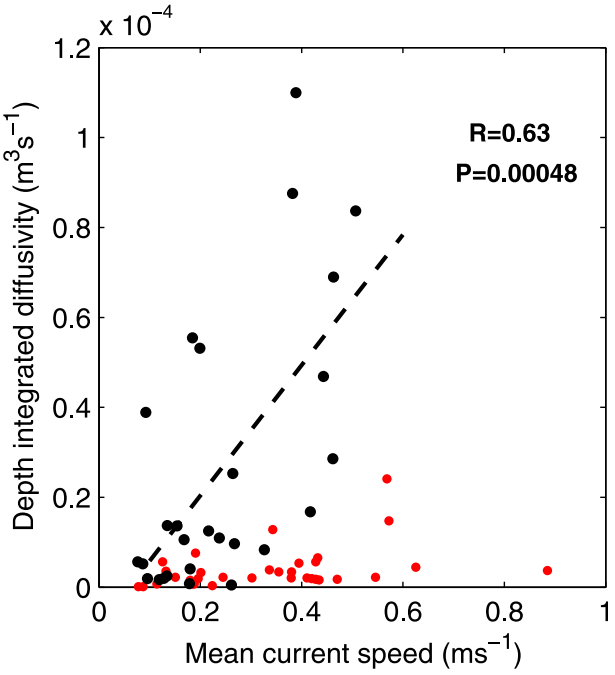

FIG. 6. Depth-integrated diffusivity (K_ρ) between 800 and 1600 m vs mean current speed in water depth shallower than 3546 m, the mean water depth in the sampling area (black), and in water depth deeper than 3546 m (red). The dashed line shows the linear fit for the shallower water data. The correlation coefficient R and P value are indicated.

mean current speed of 38 cm s^{-1} recorded by the EM-APEX floats. We also use the TOPEX/Poseidon 7.2 (TPXO7.2)[3] global tidal model to predict the tidal currents at a 1° latitudinal interval from 41° to 47°S along 70°E during the profiling time period of the EM-APEX floats. The model configuration is described in details by Egbert et al. (1994) and further by Egbert and Erofeeva (2002). Eight primary (M_2, S_2, N_2, K_2, K_1, O_1, P_1, and Q_1), two long period (M_f and M_m), and three nonlinear (M_4, MS_4, and MN_4) harmonic constituents are used to predict the tidal velocity. The predicted median tidal velocity is 1.8 cm s^{-1} at 41°S, north of the plateau, and increases to 2.6 cm s^{-1} at 47°S, on the edge of the plateau. We find that the predicted tidal flow is systematically smaller than the observed current speed within the depth range of the EM-APEX floats and that the difference between tidal and geostrophic flow decreases as we get closer to the plateau (Fig. 7). It is therefore likely that the main source of internal waves in the area is the geostrophic flow, with a small contribution from tidal motion when closer to the Kerguelen Plateau.

3) WIND SPEED

The main mechanism to transfer energy from the wind to the ocean is the generation of near-inertial internal waves that can radiate downward from the bottom of the mixed layer and subsequently break and dissipate their energy as mixing in the ocean interior (Plueddemann and Farrar 2006). For wind stress to efficiently force inertial motions in the surface mixed layer, the wind forcing must be variable and at the inertial frequency. Atmospheric frontal events, such as storms associated with atmospheric low pressure systems, can provide variable wind forcing to generate internal waves (D'Asaro 1985).

We use two diagnostics to investigate the impact of wind on mixing: the shear-to-strain variance ratio, R_ω defined in section 2, and the ratio of counterclockwise (CCW)/clockwise (CW) shear variance, hereinafter ϕ_{CCW}/ϕ_{CW}. The ϕ_{CCW}/ϕ_{CW} can be used to infer the dominant direction of energy propagation of rotationally affected internal waves (Leaman and Sanford 1975). It represents an approximate decomposition into upward- and

[3] http://volkov.oce.orst.edu/tides/global.html

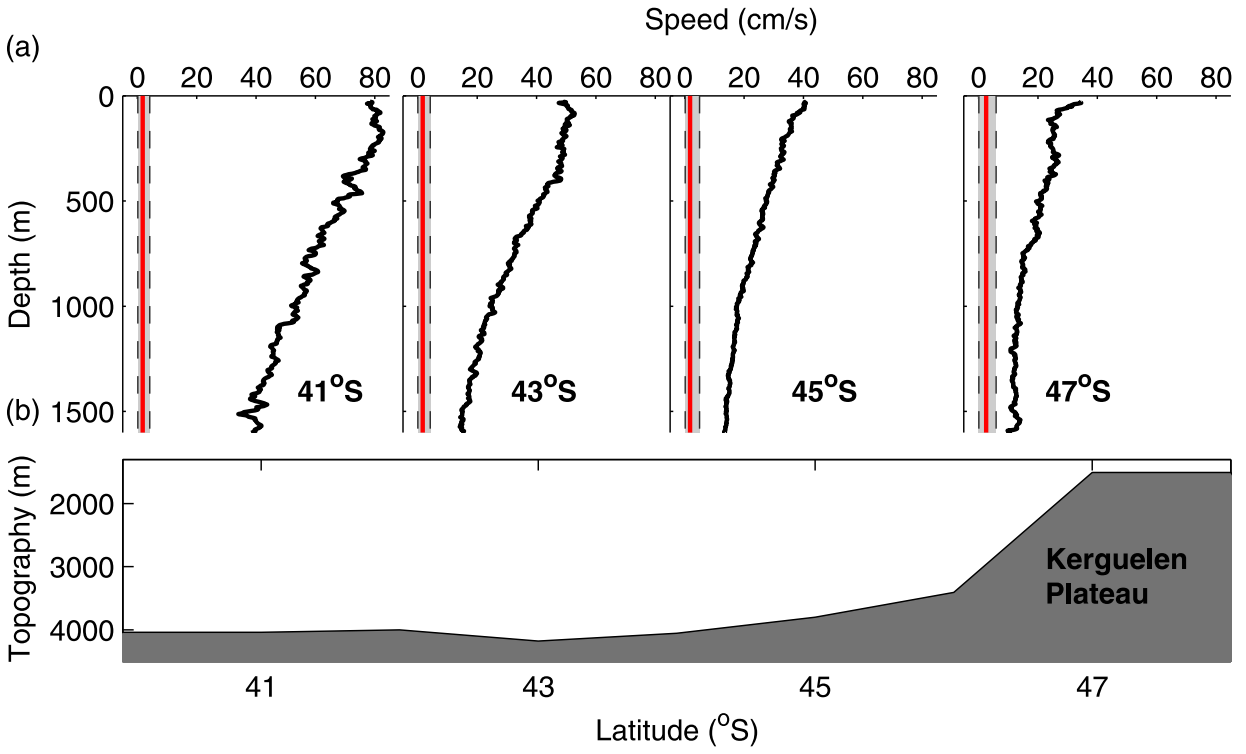

FIG. 7. (a) Vertical distribution in the upper 1600 m of TPXO-predicted median tidal speeds (red line), tidal range (black dashed lines), and EM-APEX median-observed flow speed (black curve) at 2° latitude intervals between 41° and 47°S. (b) Corresponding depth (m) of the seafloor at each latitude.

downward-propagating fields and may not be indicative of the energy flux in a multichromatic wave field. A dominance of CCW polarization of the shear suggests predominantly downward energy propagation in the Southern Hemisphere (upward phase propagation), and a dominance of CW polarization of the shear indicates that upward energy propagation dominates (downward phase propagation). We define the counterclockwise shear variance ϕ_{CCW} and the clockwise shear variance ϕ_{CW} as

$$\phi_{\mathrm{CCW}} = \frac{V_z(u/N) + V_z(v/N) + 2\mathrm{QS}}{2}, \tag{6}$$

and

$$\phi_{\mathrm{CW}} = \frac{V_z(u/N) + V_z(v/N) - 2\mathrm{QS}}{2}, \tag{7}$$

where V_z is the vertical shear, u and v are the zonal and meridional velocity components, N is the buoyancy frequency, and QS is the quadrature spectrum (Gonella 1972).

We investigate the source of enhanced mixing in the upper water column by considering profiles with integrated diffusivity values larger than $1.4 \times 10^{-5}\,\mathrm{m^3\,s^{-1}}$ in the upper 400 m. The mean vertical distribution of $\phi_{\mathrm{CCW}}/\phi_{\mathrm{CW}}$ for profiles with integrated diffusivity values larger than $1.4 \times 10^{-5}\,\mathrm{m^3\,s^{-1}}$ in the upper 400 m shows that downward energy propagation prevails in the upper 1000 m for these profiles (Fig. 8a). The mean vertical distribution of R_ω for profiles with integrated diffusivity values larger than $1.4 \times 10^{-5}\,\mathrm{m^3\,s^{-1}}$ in the upper 400 m shows enhanced values of R_ω in the upper 600 m (Fig. 8b). This suggests that regions with high diffusivity in the upper water column coincide with an increase in downward-propagating energy and near-inertial waves.

Next, we identify atmospheric frontal events that came through the Kerguelen Plateau region while the EM-APEX floats were sampling. We compute A_{wind}, the maximum wind area that we define as the surface area ($\mathrm{km^2}$) with wind speeds larger than $15\,\mathrm{m\,s^{-1}}$ within 41°–48°S and 65°–77°E. The $15\,\mathrm{m\,s^{-1}}$ threshold corresponds to the 99th percentile of the wind field within 41°–48°S and 65°–77°E during the EM-APEX sampling period. We use CERSAT, a blended satellite-derived wind product provided by European Remote Sensing Satellite Processing and Archiving Facility at the French Research Institute for Exploitation of the Sea.[4] The wind data are provided

[4] ftp://ftp.ifremer.fr/ifremer/cersat/products/gridded/mwf-blended/data/6-hourly/

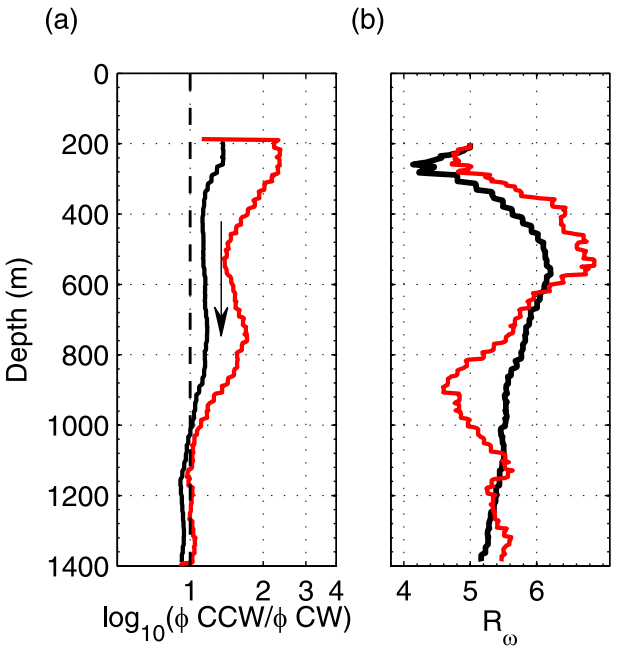

FIG. 8. Mean vertical profiles of (a) ϕ_{CCW}/ϕ_{CW} and (b) shear-to-strain variance ratio (R_ω) as a function of depth over whole dataset (black) and for profiles with vertically integrated diffusivity values larger than $1.4 \times 10^{-5}\,m^3\,s^{-1}$ in the upper 400 m (red). ϕ_{CCW}/ϕ_{CW} values greater than one (dotted–dashed line) suggest downward energy propagation as indicated by the arrow in (a).

at 6-hourly intervals at 0.25° × 0.25° resolution. We expect large values of A_{wind} to be associated with significant atmospheric frontal events that can generate near-inertial waves. As such, A_{wind} could be a diagnostic for intense surface mixing events. Over the 10 weeks of observations, we identify the two main atmospheric frontal systems beginning on 23 November 2008 and on 29 December 2009. After the passage of the atmospheric frontal systems, the upper water column–integrated diffusivity reaches values well above average levels (Fig. 9b). The mean vertical ϕ_{CCW}/ϕ_{CW} ratio shows that integrated diffusivity peaks are followed by enhanced downward internal wave propagation with a delay of 2 to 5 days (Fig. 9b).

To determine if the peaks in integrated diffusivity are because of the wind, we would ideally use local wind observations correlating wind stress or wind work with mixing observed in the upper ocean. Since there are no direct wind observations along the trajectories of the floats, we use the 6-hourly, 0.25° × 0.25° resolution CERSAT wind product that impose significant temporal and spatial limitations on the analysis. We find no direct correlation between the diffusivity and corresponding wind stress. One possible reason for the lack of correlation is that the resolution of wind stress estimates from satellite-derived wind data is too coarse to relate wind stress and variations in mixing estimates.

We suggest there is some evidence of wind-driven mixing in the upper 800 m below the mixed layer in the form of downward-propagating near-inertial internal waves. The enhanced surface mixing is attributed to large atmospheric frontal events. The time lag, which can vary from 10 to 20 days (Balmforth and Young 1999), and other dynamics between wind forcing, the generation of near-inertial waves, their breaking, and resulting enhanced mixing make showing the relationship between wind and mixing difficult. Forcing a slab mixed layer model with the CERSAT wind product, the flux from wind to inertial motions could be estimated and compared with observed mixing in the upper ocean (Pollard and Millard 1970; D'Asaro 1985; Alford 2003). Such an analysis will be the focus of future work.

d. Regional variability of mixing

Fronts are regions of sharp transitions of ocean properties. Previous studies in the Southern Ocean have shown frontal regions enhancing mixing along the Antarctic Circumpolar Current pathway (Sloyan 2005), as well as enhancing upper-ocean mixing north of an Antarctic Circumpolar Current front (Thompson et al. 2007; Sloyan et al. 2010). In this study, the SAF/STF region separates the Subantarctic zone from the Polar Front zone (Fig. 1).

The mean mixing intensity in the Subantarctic zone, in the Polar Front zone, and within the SAF/STF region differs by as much as an order of magnitude (Table 1). Overall, mixing is more intense within the SAF/STF region than in the Subantarctic zone or in the Polar Front zone (Fig. 10a). The weakest mixing is in the Subantarctic zone (Table 1; Fig. 10a). All three regions reach a maximum mixing value below 700 m, while subsurface minima are located between 250 and 450 m (Fig. 10a). We also find that the mean value of dissipation rate varies whether at the western end or at the eastern end of the SAF/STF region. The mean dissipation rate in the SAF/STF region west of 69°E is $7.2 \times 10^{-10}\,W\,kg^{-1}$, while east of 71°E, the mean dissipation rate is $34 \times 10^{-10}\,W\,kg^{-1}$. This could be the result of internal wave generation and breaking as the flow impinges on the rough topography of the plateau, enhancing mixing downstream from the plateau but not upstream.

The mean shear-to-strain variance ratio R_ω is similar in the SAF/STF region and in the Polar Front zone, while the mean R_ω values in the Subantarctic zone are higher (Table 1). This difference is enhanced below 400 m, where the mean $R_\omega = 5.3$ both in the Subantarctic zone and the SAF/STF region and $R_\omega = 6.7$ in the Subantarctic zone (Fig. 10b). This suggests that near-inertial frequency waves are more present in the Subantarctic

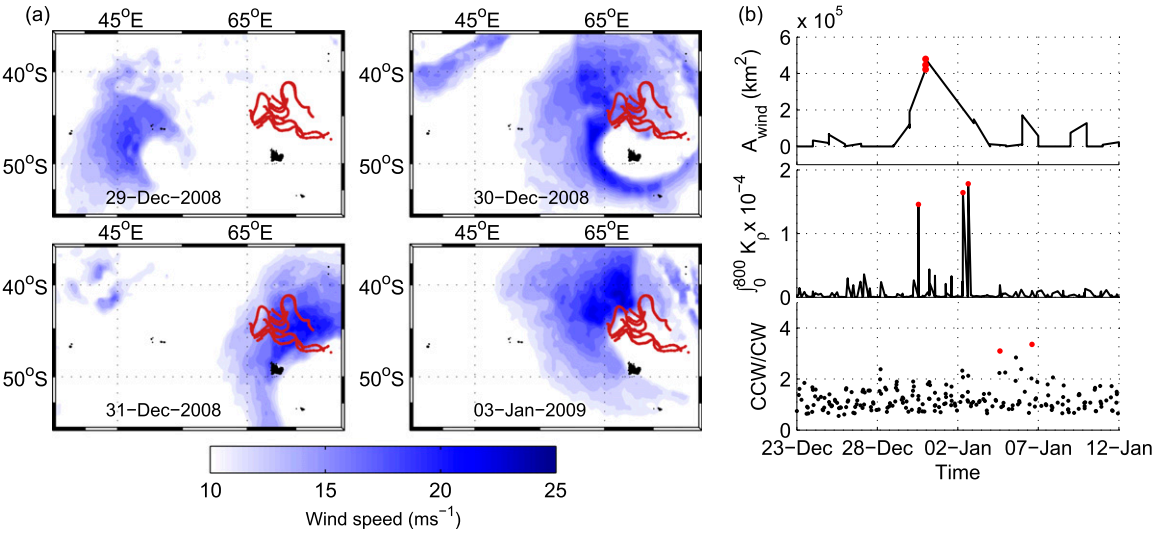

FIG. 9. (a) Evolution of one of the identified atmospheric frontal systems; surface wind speed maps are shown (color scale) between 29 Dec 2008 and 3 Jan 2009 in the Kerguelen Plateau region with EM-APEX float trajectories (red). To highlight the atmospheric frontal system, surface wind speeds below 10 m s^{-1} are not shown. Wind speeds are from blended CERSAT satellite data. (b) Subset time series for the same atmospheric frontal system of (top) A_{wind} the maximum wind area, (middle) vertically integrated diffusivity (K_ρ) in the upper 800 m, and (bottom) corresponding mean vertical $\phi_{\text{CCW}}/\phi_{\text{CW}}$ between 23 Dec 2008 and 12 Jan 2009. Values above the overall mean of the dataset are highlighted (red).

zone than in the other regions. We compare values of the shear-to-strain variance ratio from this study and previous studies in Table 2. The $\phi_{\text{CCW}}/\phi_{\text{CW}}$ ratio used to distinguish upward from downward energy propagation varies substantially from one region to another. In the SAF/STF region, where we expect upward-propagating internal waves to dominate, $\phi_{\text{CCW}}/\phi_{\text{CW}}$ is greater than one, implying the presence of downward-propagating internal waves. The analysis of internal waves shows that 62% of observed internal waves in the area are propagating downward (Meyer et al. 2015, unpublished manuscript). The mean depth in the SAF/STF region is 3535 m, and it is likely that many upward-propagating internal waves dissipate before they reach 1600-m depth. Since we only sample the upper 1600 m of the water column, such waves might be underrepresented compared with what would have been observed if we had full depth data. We expect upward-propagating internal waves to be better sampled in the Polar Front zone since its mean depth is 119 m shallower than the SAF/STF region mean depth (Table 1). The Polar Front zone has $\phi_{\text{CCW}}/\phi_{\text{CW}}$ values less than one below 300 m, which suggests that some of the energy in the Polar Front zone comes from upward-propagating internal waves (not shown).

A key point is that mixing is substantially enhanced within the SAF/STF region (Fig. 10), particularly downstream of the Kerguelen Plateau. The variability of mixing north of, within, and south of the front suggests that different regional dynamics influence mixing. In the SAF/STF region, intense current speeds and interactions with rough topography are associated with enhanced turbulent mixing [section 4c(2)]. We find that mixing dynamics in the Subantarctic zone with low topographic roughness are controlled by wind-generated inertial motions [section 4c(3)]. In the Polar Front zone,

TABLE 1. Values of mean mixing and mean environmental parameter in the Polar Front zone within the SAF/STF region and in the Subantarctic zone.

Parameter	Polar Front zone	SAF/STF region	Subantarctic zone
Depth (m)	3416	3535	3815
Diffusivity (m^2 s^{-1})	2.0×10^{-5}	6.0×10^{-5}	0.5×10^{-5}
Current speed (m s^{-1})	0.17	0.44	0.15
Shear (s^{-1})	1.5×10^{-4}	3.5×10^{-4}	1.0×10^{-4}
Topographic roughness (m^2)	1.9×10^{-4}	2.0×10^{-4}	1.8×10^{-4}
Shear-to-strain ratio	5.2	5.1	6.2
$\phi_{\text{CCW}}/\phi_{\text{CW}}$ ratio	0.9	1.3	1.1
Wind stress (N m^{-2})	1.33	1.54	1.97

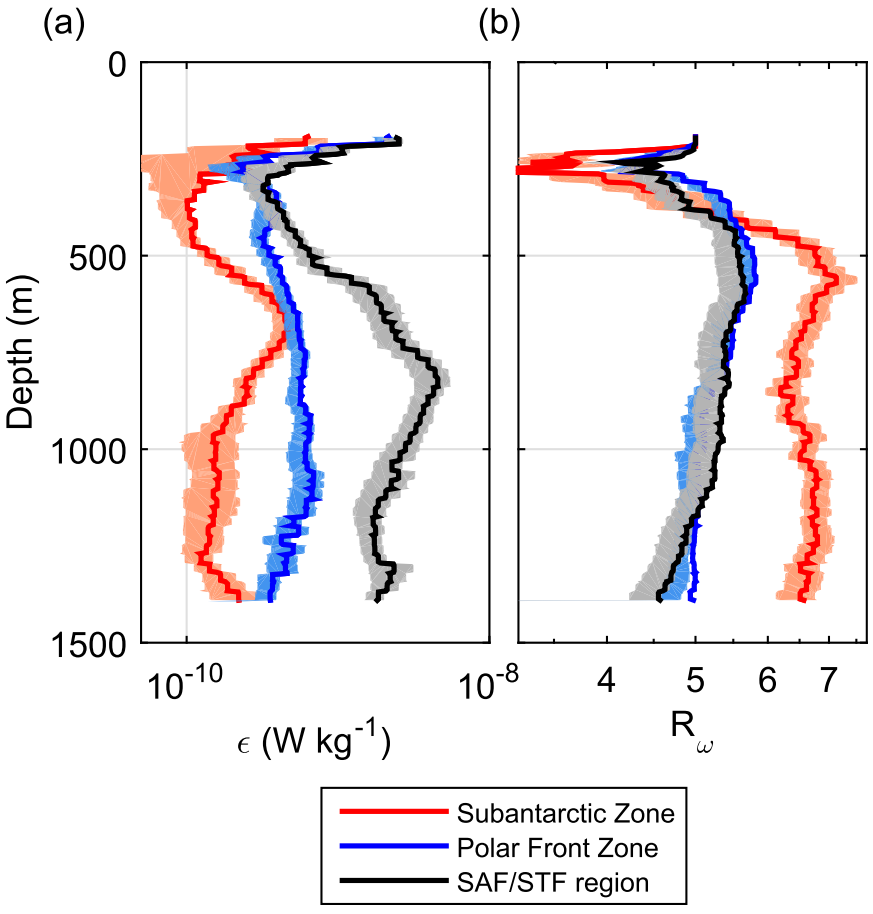

FIG. 10. Mean vertical profile of (a) diapycnal diffusivity and (b) shear-to-strain variance ratio (R_ω), as a function of depth in the Subantarctic zone (red), Polar Front zone (blue), and SAF/STF region (black). Shaded areas show the 90% confidence intervals computed as the standard deviation from bootstrap sampling.

we find that the combination of the Kerguelen Plateau and associated rough topography with moderate currents leads to substantial mixing [section 4c(1)].

This regional variability of mixing is consistent with the internal wave analysis of the same dataset. The distribution of internal waves shows that in the SAF/STF region, the interaction of the topography and the strong current generates upward-propagating internal waves, while away from topography in the Subantarctic zone, wind forcing is the source of downward-propagating near-inertial internal waves (Meyer et al. 2015, unpublished manuscript).

5. Discussion

a. *Enhanced mixing in an eddy*

In the upper 400 m of the edge of the cyclonic eddy, we observe large, integrated dissipation values, up to 10 times larger than mixing elsewhere (Fig. 11). Altogether, 18 profiles with large values of mixing were sampled over a two-week period by three EM-APEX floats in different sections of the eddy. The large mixing values occur 10 days after the passing of the first atmospheric frontal system identified in section 4c(3). A few other profiles show similar enhanced mixing in the upper 400 m away from the eddy but are not gathered as closely together. We explore several theories that could explain the intense mixing we see close to the surface at the edge of the eddy.

Enhanced mixing in the upper water column is often attributed to breaking near-inertial internal waves generated at the ocean surface by atmospheric forcing. The 10-day-long delay between the atmospheric frontal system and the large mixing values are consistent with observed time scales of the transmission of near-inertial waves from the mixed layer into the ocean's interior (Balmforth and Young 1999). Various interactions

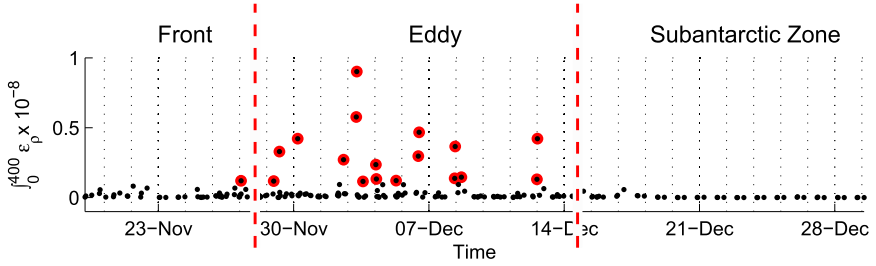

FIG. 11. Time evolution of depth-integrated dissipation ε in the upper 400 m for a subset of profiles sampled between 19 Nov 2008 and 29 Dec 2008. The red vertical dashed lines separate profiles by regions in which they were sampled (SAF/STF region, eddy, or Subantarctic zone). The 18 profiles with values of integrated dissipation larger than 0.1×10^{-8} are highlighted (red points).

between near-inertial waves and the flow of the eddy or wave–mean flow interactions can explain an increase in the rate of near-inertial wave breaking and enhanced mixing:

1) Wave trapping: Theory suggests that wind-forced, near-inertial internal waves are vertically amplified in regions of negative relative vorticity gradients, leading to a quick decay with time, wave breaking, and enhanced local dissipation rate (Kunze 1985). Both observational (Elipot et al. 2010) and modeling (van Meurs 1998; Balmforth and Young 1999) studies have shown that near-inertial internal waves can decay more rapidly when exposed to strong relative vorticity gradients. Jing and Wu (2013) found enhanced mixing under anticyclonic eddies in the Northern Hemisphere, invoking negative relative vorticity as being responsible.
2) Near-inertial chimney: From a three-dimensional numerical model, Lee and Niiler (1998) developed the concept of near-inertial chimneys where in regions of negative relative vorticity such as the core of anticyclonic eddies, downward-propagating near-inertial waves get funneled down the core and then trapped at a critical layer where near-inertial energy reaches its maximum.
4) Wave capture: Nonlinear interactions between internal waves and eddies can lead to wave capture, rapid wave breaking, and dissipation (Bühler and McIntyre 2005). Taking the limit in which the group velocity of an internal wave is much smaller than the background flow provides a partial analogy with the filamentation of a passive tracer (Bühler and McIntyre 2005). In the case of wave capture, the deformation rate of strain exceeds relative vorticity, and therefore the wavelengths and group velocity of an internal wave decreases to zero, while the amplitude increases exponentially, leading to the dissipation of the wave.

To look at the potential role of relative vorticity in enhancing mixing in the eddy, we estimate the local weekly mean vertical component of the relative vorticity $\zeta = (\partial v/\partial x - \partial u/\partial y)$, where u and v are the components of the horizontal velocity vector in the zonal and meridional directions from the satGEM velocity fields. We set the horizontal scales to $\partial x = \partial y = 50$ km and regrid the satGEM velocity fields on those scales. The resulting smoothed weekly maps of mean relative vorticity show the cyclonic eddy has the largest positive relative vorticity values in the area (not shown). With such strong positive relative vorticity in the eddy, we discard the first hypothesis of wave trapping driven by negative relative vorticity. We also discard the second hypothesis of a near-inertial chimney as this can only take place in the core of anticyclonic eddies.

We look at the vertical mixing distribution in the 18 profiles and find that mixing is enhanced in the upper 300 m. Using results from an analysis of the internal wave field for this dataset (Meyer et al. 2015, unpublished manuscript), we see that the 18 profiles with enhanced mixing are associated with four internal waves. All four waves are propagating downward and have near-inertial intrinsic frequencies. When we compare these four waves with the nine other internal waves observed in the eddy, the four waves are shallower, have shorter vertical wavelength, and slower group velocity.

The characteristics of the observed waves satisfy the theory of wave capture by the mean flow Eq. (4), where vertical wavelength and group velocity decrease until the waves dissipate. We suggest that the observed enhanced mixing on the edge of the eddy is the result of internal wave capture by the mean flow of the eddy.

b. *Water mass transformation rates*

There is growing evidence that turbulent mixing in the Southern Ocean may control the deep-ocean stratification and the global overturning circulation. Transformation of deep water in the Southern Ocean closes the global overturning circulation (Sloyan and Rintoul 2001). Quantifying the role of turbulent mixing on water mass transformation is key to understanding the global overturning (Nikurashin and Ferrari 2013).

TABLE 2. Location, sampling range, measured (mean, range or latitude) or assumed value of the shear-to-strain variance ratio (R_ω) in previous studies and in this study.

Reference	Location	Sampling range (m)	Measured R_ω	Assumed R_ω
Garrett and Munk (1975)	North Atlantic Ocean	0–1300	3 (mean)	—
Polzin et al. (2003)	Midlatitude	0–800	5–11 (range)	—
Naveira Garabato et al. (2004b)	Nordic Seas	0–5000	8–14 (range)	—
Sloyan (2005)	Southern Ocean	—	—	3
Kunze et al. (2006)	Global abyssal mean	0–5000	7	—
Thompson et al. (2007)	Drake Passage	—	—	10
Fer et al. (2010)	Arctic	0–500	11 (mean)	—
Jing and Wu (2010)	Northwestern Pacific	—	—	7
Wu et al. (2011)	Southern Ocean	—	—	7
Whalen et al. (2012)	Global	—	—	3
Jing and Wu (2013)	Hawaii	—	—	3
MacKinnon et al. (2013)	Pacific Ocean	0–1000	3.9 at 25.5°N	—
		0–1000	5.3 at 27.8°N	—
		0–1000	4.1 at 28.9°N	—
		0–1000	8.2 at 30.1°N	—
		0–1000	5.1 at 32.9°N	—
		0–1000	9.8 at 37.1°N	—
This study	Kerguelen Plateau	0–1600	1–19 (range)	—
	45°S		5.6 (mean)	

We investigate the impact of mixing on local water masses by estimating the dissipation rate with respect to potential density for the whole area and each dynamical region (Table 3). In the EM-APEX depth range (upper 1600 m), dissipation is largest at depths corresponding to AAIW. Nearly 50% of the total dissipation estimated in the data occurs in AAIW, while 20% is in SAMW and 31% is in UCDW. Overall, the SAF/STF region is the region where most of the mixing of water masses takes place. The Polar Front zone also plays an important role, with a significant percentage of the total dissipation found in the Polar Front zone for each water mass. The eddy is associated with strong dissipation in the shallow SAMW. In the Subantarctic zone, dissipation within each water mass is weak. The depth range of the mixing estimates (200–1400 m) does not allow an assessment of dissipation in UCDW in the Subantarctic zone. In summary, most of the mixing of water masses in the upper 1600 m affects the AAIW and UCDW and takes place in the SAF/STF region and Polar Front zone.

In the context of the Southern Ocean overturning circulation, we infer the diapycnal transformation rate of water masses in the upper 1600 m in terms of potential density using our in situ estimate of diffusivity. Following the water mass transformation framework developed by Walin (1982), the diapycnal volume flux or transformation D is

$$D(\rho) = -\frac{1}{\delta\rho}\int_{\rho} K_\rho \frac{\partial\rho}{\partial z} dA\,, \tag{8}$$

where K_ρ is the observed diffusivity at the density level ρ, $\partial\rho/\partial z$ is the observed gradient in density around K_ρ, and A is the area of the density surface ρ based on the *World Ocean Atlas* (Levitus and Boyer 1994). We first apply Eq. (8) to the Kerguelen Plateau region (40°–50°S and 67°–78°E), estimating the diapycnal transformation for the Subantarctic zone, the SAF/STF region, and the Polar Front zone (Fig. 12a). Density levels and latitudinal boundaries for the density surfaces are shown in Fig. 12. Observed diffusivities in the Kerguelen region lead to a peak in transformation upgradient in the SAF/STF region of 0.28 Sverdrups (Sv; $1\,\text{Sv} \equiv 10^6\,\text{m}^3\,\text{s}^{-1}$) at $\rho = 27.5\,\text{kg}\,\text{m}^{-3}$, which is the boundary between AAIW and UCDW. We also scale the inferred diapycnal transformation to the entire Southern Ocean

TABLE 3. Percentage for each dynamical region of the total dissipation ε estimated in the upper 1600 m from EM-APEX floats associated with each water mass. SAMW is defined as $\sigma_\theta \le 27.1\,\text{kg}\,\text{m}^{-3}$, AAIW is defined as $27.1 \le \sigma_\theta \le 27.5\,\text{kg}\,\text{m}^{-3}$, and UCDW is defined as $\sigma_\theta \ge 27.5\,\text{kg}\,\text{m}^{-3}$.

Water mass	Entire region	Polar Front zone	SAF/STF region	Subantarctic zone	Eddy
SAMW	20	4.4	4	1.2	10.4
AAIW	48	11.52	32.16	1.44	2.88
UCDW	31	14.57	15.81	—	0.62

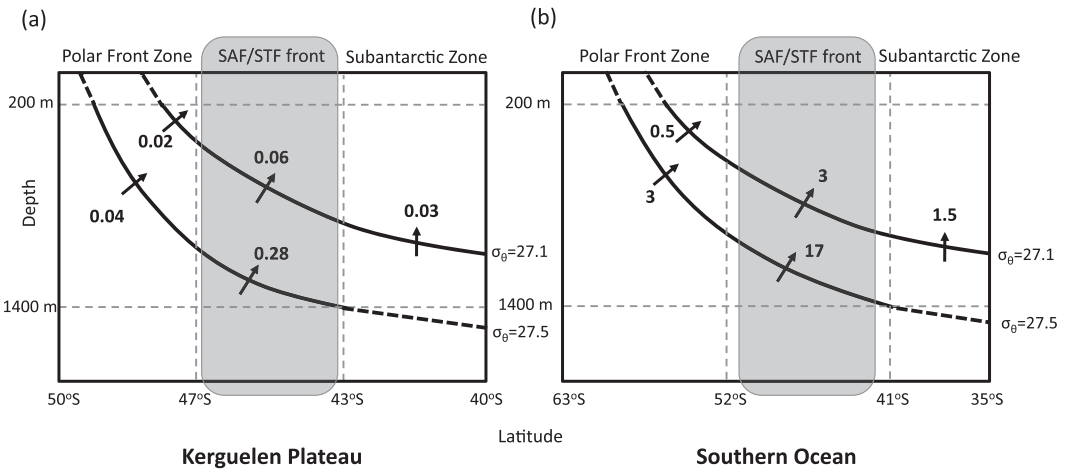

FIG. 12. Schematic of the inferred diapycnal transformation rates for (a) the Kerguelen Plateau region (40°–50°S and 67°–78°E) and (b) scaled to the entire Southern Ocean (40°–63°S). The transformation rates (Sv) are based on estimates of diffusivity from the EM-APEX floats and the area of density surfaces (ρ_θ; kg m^{-3})from the *World Ocean Atlas* (Levitus and Boyer 1994). The latitudinal boundaries of the Polar Front zone, the SAF/STF region (highlighted in gray), and the Subantarctic zone boundaries are shown (gray dashed line). Transformation rates as inferred in the sampling range of the EM-APEX floats between 200 and 1400 m.

(40°–63°S), using the observed diffusivities from the Kerguelen Plateau region (Fig. 12b). The resulting diapycnal transformation estimates are significant for the Southern Ocean overturning circulation budget with an overall value of 20 Sv of upgradient transformation of denser waters along the 27.5 kg m^{-3} isopycnal surface, of which 17 Sv takes place in the SAF/STF region (Fig. 12b). The mean roughness in the circumpolar band between 40° and 50°S in the Southern Ocean (2.4×10^4 m^2) is larger than the mean roughness (1.4×10^4 m^2) in our dataset area north of the Kerguelen Plateau (40°–50°S, 67°–78°E). The observed mean mixing values north of the Kerguelen Plateau are therefore not likely to be particularly high because of topographic roughness compared to the rest of the Southern Ocean, and it is reasonable to extrapolate them to the entire Southern Ocean. We have also carefully chosen the latitude bands to include the same fronts in the Kerguelen Plateau region and in the Southern Ocean extrapolation. The dynamics of the mixing generation between the fronts and the topography in the Southern Ocean will, however, vary from those we observed north of the Kerguelen Plateau, and such variations are not taken into account in the Southern Ocean extrapolation. Applying to all available observed diffusivity profiles in the Southern Ocean, this method of estimating water mass transformation rates would decrease the uncertainties associated with the Southern Ocean extrapolation.

The 20-Sv circumpolar estimate of water mass transformation at $\rho = 27.5$ kg m^{-3} is a factor of 3 to 4 larger than recent estimates such as 7 (Badin et al. 2013) and 5 Sv (Nikurashin and Ferrari 2013) at $\gamma = 27.5$ kg m^{-3}. These results suggest that water mass transformation due to diapycnal mixing is dominant in the SAF/STF region, over rough topography, and at the boundary between UCDW and AAIW. Enhanced transformation in the front is consistent with recent work (Badin et al. 2013) and previous studies showing enhanced mixing in frontal regions (e.g., Sloyan 2005; Naveira Garabato et al. 2007; Thompson et al. 2007; St. Laurent et al. 2012). Our estimate of the upgradient transformation of the water masses from a region with high mixing values, particularly in this density range between the Subantarctic Front and Polar Front, is evidence that topographic features and the Antarctic Circumpolar Current play a significant role in driving the Southern Ocean overturning budget. Lower background mixing could not provide the required water mass transformations.

c. *Validating the shear-to-strain parameterization method*

For validation, we compare the dissipation rate estimates from the EM-APEX floats with measurements from a microstructure profiler. Free-falling vertical microstructure profiler measurements were collected during the SOFine survey in conjunction with the deployment of the EM-APEX floats (Waterman et al. 2013). The EM-APEX floats provided 914 profiles between November 2008 and January 2009, while 42 profiles were sampled with a microstructure profiler between November and December 2008 (Fig. 1). The mean vertical profiles of the dissipation rate from the EM-APEX and from the vertical microstructure profiler are within an order of magnitude and have a similar vertical structure, indicating

that the finescale parameterization applied to the EM-APEX data is appropriate (Fig. 13). Having many profiles from the EM-APEX floats means that less vertical averaging is required, and thus the vertical profile of dissipation has more detail about the levels of dissipation with depth than the vertical profile of dissipation from the microstructure profiler (Fig. 13). The microstructure measurements, which make no assumption about mixing sources, and the finescale parameterization estimates, which infer mixing from internal waves, agree well. Taking into account the sampling differences and the uncertainties associated with the shear–strain finescale parameterization, it is remarkable that the two dissipation rate profiles have such similar vertical structures.

Waterman et al. (2014) identified potential limitations of the finescale parameterization method using shipboard data from the same survey. Finescale parameterization estimates from shipboard lowered acoustic Doppler current profiler data overpredicted dissipation rates compared to microstructure rates within the bottom 1 km in regions of internal wave generation. In our study, the EM-APEX data have a much higher vertical resolution of horizontal velocity (3 m) than lowered acoustic Doppler current profiler data (20 m), making them more suitable for estimating mixing rates. The EM-APEX enables us to resolve the cutoff wavenumber of the spectra used to estimate mixing and therefore to integrate the variance of the shear and strain at the correct wavelengths. The EM-APEX float profiles are on average 2000 m off the seafloor, well above the depths where the overestimates of mixing were found by Waterman et al. (2014). We therefore have confidence that our mixing estimates are robust.

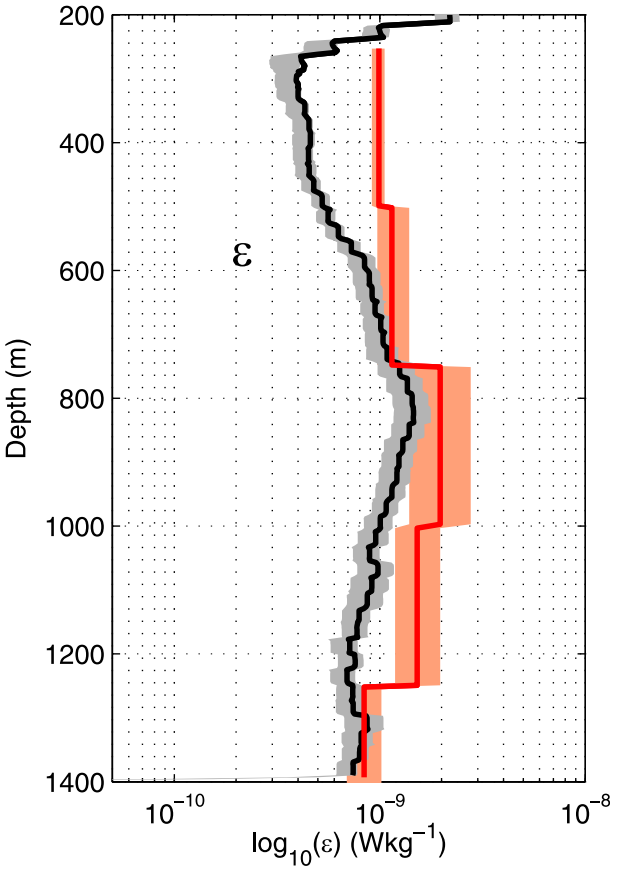

FIG. 13. Mean vertical profile of the dissipation rate ϵ from the EM-APEX data (black) and from microstructure profiler data (red; from Waterman et al. 2013) as a function of depth. Shaded areas shows the 90% confidence intervals computed via standard deviation using bootstrap sampling.

6. Conclusions

We show that observed mixing values north of the Kerguelen Plateau in the Southern Ocean have significant spatial and temporal variability. This variability is consistent with an internal wave analysis of the same dataset (Meyer et al. 2015, unpublished manuscript). Robust internal wave and mixing patterns linked to several regional processes are identified and summarized in Fig. 14. Rough topography is associated with mixing values 3 times higher than values associated with smooth topography. The most intense mixing is observed in the SAF/STF region, which also advects internal wave energy and momentum away from the generation site (Meyer et al. 2015, unpublished manuscript). We suggest that enhanced mixing in the area is the result of breaking internal waves generated at the seafloor by the interaction of strong currents with rough topography either upstream from the Kerguelen Plateau or at the plateau. We infer that in the Southern Ocean there is substantial water mass transformation of 17 Sv taking place in the SAF/STF region, at the boundary between UCDW and AAIW. The observation of intense bursts of mixing in an eddy highlights the impact of mean–flow interactions on the dynamics of internal waves. In the region north of the SAF/STF region, large atmospheric frontal zones seem to regulate wind-driven mixing in the upper 800 m of the ocean. Clearly, the role of regional dynamics in the distribution and intensity of mixing requires more attention.

Acknowledgments. We thank the scientists and crew from the RRS *James Cook JC029*. We acknowledge the valuable contributions of the SOFine team, S. Waterman and A. Naveira Garabato in particular for providing advice and data on numerous occasions. We thank B. Pena-Molino and M. Nikurashin for valuable discussions. We also thank two anonymous reviewers whose comments improved this paper. AM was supported

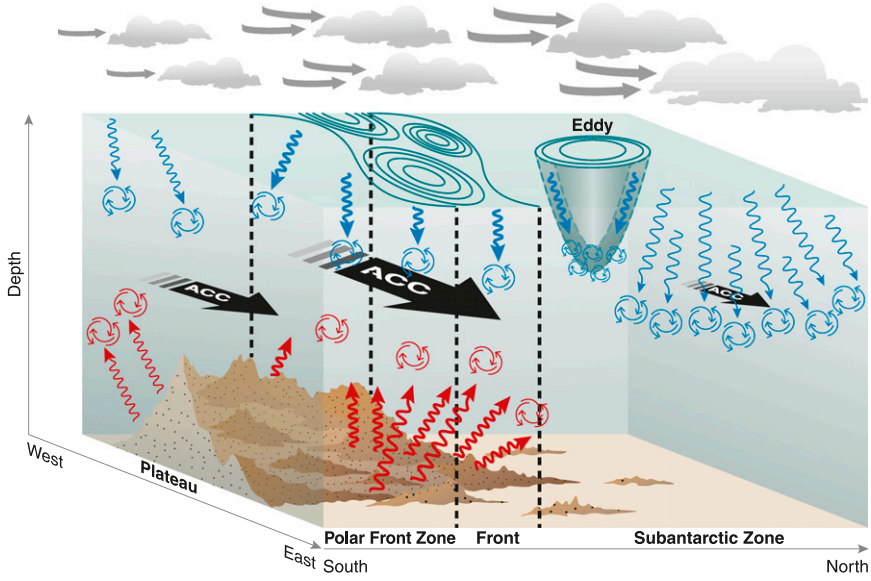

FIG. 14. Schematic of the spatial distribution of internal waves, mixing, and associated processes north of the Kerguelen Plateau. The SAF/STF region separates two dynamical zones. In the Polar Front zone, mixing intensities are controlled by topographic roughness generating upward-propagating internal waves (red arrows). In the SAF/STF region, strong flow over rough topography is associated with high mixing values and with upward-propagating internal waves that are advected away from the generation site. In the Subantarctic zone, stronger wind forcing generates near-inertial downward-propagating internal waves (blue arrows). Mesoscale eddy activity associated with enhanced mixing is observed north of the SAF/STF region.

by the joint CSIRO–University of Tasmania Quantitative Marine Science (QMS) program and the 2009 CSIRO Wealth from Ocean Flagship Collaborative Fund. BMS was supported by the Australian Climate Change Science Program, jointly funded by the Department of the Environment and CSIRO. KLPs salary support was provided by Woods Hole Oceanographic Institution bridge support funds. We thank J. Dunlap, S. Rintoul, S. Wijffels, and B. Owens for their support for the EM-APEX component of the SOFine project. Funding for the EM-APEX experiment was provided by the Australian Research Council Discovery Project (DP0877098) and Australian Government DEWHA Projects 3002 and 3228.

REFERENCES

Alford, M. H., 2001: Internal swell generation: The spatial distribution of energy flux from the wind to mixed layer near-inertial motions. *J. Phys. Oceanogr.,* **31,** 2359–2368, doi:10.1175/1520-0485(2001)031<2359:ISGTSD>2.0.CO;2.

——, 2003: Improved global maps and 54-year history of wind-work on ocean inertial motions. *Geophys. Res. Lett.,* **30,** 1424, doi:10.1029/2002GL016614.

——, and M. C. Gregg, 2001: Near-inertial mixing: Modulation of shear, strain and microstructure at low latitude. *J. Geophys. Res.,* **106,** 16 947–16 968, doi:10.1029/2000JC000370.

——, J. A. MacKinnon, Z. Zhao, R. Pinkel, J. Klymak, and T. Peacock, 2007: Internal waves across the Pacific. *Geophys. Res. Lett.,* **34,** L24601, doi:10.1029/2007GL031566.

——, M. C. Gregg, V. Zervakis, and H. Kontoyiannis, 2012: Internal wave measurements on the Cycladic Plateau of the Aegean Sea. *J. Geophys. Res.,* **117,** C01015, doi:10.1029/2011JC007488.

Badin, G., R. G. Williams, Z. Jing, and L. Wu, 2013: Water mass transformations in the Southern Ocean diagnosed from observations: Contrasting effects of air–sea fluxes and diapycnal mixing. *J. Phys. Oceanogr.,* **43,** 1472–1484, doi:10.1175/JPO-D-12-0216.1.

Balmforth, N. J., and W. R. Young, 1999: Radiative damping of near-inertial oscillations in the mixed layer. *J. Mar. Res.,* **57,** 561–584, doi:10.1357/002224099321549594.

Belkin, I. M., and A. L. Gordon, 1996: Southern Ocean fronts from the Greenwich meridian to Tasmania. *J. Geophys. Res.,* **101,** 3675–3696, doi:10.1029/95JC02750.

Bell, T. H., 1975: Topographically generated internal waves in the open ocean. *J. Geophys. Res.,* **80,** 320–327, doi:10.1029/JC080i003p00320.

Bray, N. A., and N. P. Fofonoff, 1981: Available potential-energy for mode eddies. *J. Phys. Oceanogr.,* **11,** 30–47, doi:10.1175/1520-0485(1981)011<0030:APEFME>2.0.CO;2.

Bryan, F., 1987: Parameter sensitivity of primitive equation ocean general-circulation models. *J. Phys. Oceanogr.,* **17,** 970–985, doi:10.1175/1520-0485(1987)017<0970:PSOPEO>2.0.CO;2.

Bühler, O., and M. E. McIntyre, 2005: Wave capture and wave–vortex duality. *J. Fluid Mech.,* **534,** 67–95, doi:10.1017/S0022112005004374.

Cairns, J. L., and G. O. Williams, 1976: Internal wave observations from a midwater float, 2. *J. Geophys. Res.,* **81,** 1943–1950, doi:10.1029/JC081i012p01943.

Damerell, G. M., K. J. Heywood, D. P. Stevens, and A. C. N. Garabato, 2012: Temporal variability of diapycnal mixing in shag rocks passage. *J. Phys. Oceanogr.,* **42,** 370–385, doi:10.1175/2011JPO4573.1.

——, ——, and ——, 2013: Direct observations of the Antarctic Circumpolar Current transport on the northern flank of the Kerguelen Plateau. *J. Geophys. Res. Oceans,* **118,** 1333–1348, doi:10.1002/jgrc.20067.

D'Asaro, E. A., 1985: Upper ocean temperature structure, inertial currents, and Richardson number observed during strong meteorological forcing. *J. Phys. Oceanogr.,* **15,** 943–962, doi:10.1175/1520-0485(1985)015<0943:UOTSIC>2.0.CO;2.

——, and R. C. Lien, 2000: The wave–turbulence transition for stratified flows. *J. Phys. Oceanogr.,* **30,** 1669–1678, doi:10.1175/1520-0485(2000)030<1669:TWTTFS>2.0.CO;2.

Deacon, G. E. R., 1937: *The Hydrology of the Southern Ocean.* Discovery Rep. Series, Vol. 15, Cambridge University Press, 124 pp.

Egbert, G. D., and R. D. Ray, 2000: Significant dissipation of tidal energy in the deep ocean inferred from satellite altimeter data. *Nature,* **405,** 775–778, doi:10.1038/35015531.

——, and S. Y. Erofeeva, 2002: Efficient inverse modelling of barotropic ocean tides. *J. Atmos. Oceanic Technol.,* **19,** 183–204, doi:10.1175/1520-0426(2002)019<0183:EIMOBO>2.0.CO;2.

——, A. F. Bennett, and M. G. G. Foreman, 1994: TOPEX/POSEIDON tides estimated using a global inverse model. *J. Geophys. Res.,* **99,** 24 821–24 852, doi:10.1029/94JC01894.

Elipot, S., R. Lumpkin, and G. Prieto, 2010: Modification of inertial oscillations by the mesoscale eddy field. *J. Geophys. Res.,* **115,** C09010, doi:10.1029/2009JC005679.

Fer, I., P. Nandi, W. S. Holbrook, R. W. Schmitt, and P. Paramo, 2010: Seismic imaging of a thermohaline staircase in the western tropical North Atlantic. *Ocean Sci.,* **6,** 621–631, doi:10.5194/os-6-621-2010.

Ferrari, R., 2014: What goes down must come up. *Nature,* **513,** 179–180, doi:10.1038/513179a.

Garrett, C., and W. Munk, 1972: Oceanic mixing by breaking internal waves. *Deep-Sea Res. Oceanogr. Abstr.,* **19,** 823–832, doi:10.1016/0011-7471(72)90001-0.

——, and ——, 1975: Space-time scales of internal waves: A progress report. *J. Geophys. Res.,* **80,** 291–297, doi:10.1029/JC080i003p00291.

Goff, J. A., and T. H. Jordan, 1988: Stochastic modeling of seafloor morphology: Inversion of sea beam data for second-order statistics. *J. Geophys. Res.,* **93,** 13 589–13 608, doi:10.1029/JB093iB11p13589.

Gonella, J., 1972: Rotary-component method for analyzing meteorological and oceanographic vector time series. *Deep-Sea Res. Oceanogr. Abstr.,* **19,** 833–846, doi:10.1016/0011-7471(72)90002-2.

Gregg, M. C., 1987: Diapycnal mixing in the thermocline: A review. *J. Geophys. Res.,* **92,** 5249–5286, doi:10.1029/JC092iC05p05249.

——, 1989: Scaling turbulent dissipation in the thermocline. *J. Geophys. Res.,* **94,** 9686–9698, doi:10.1029/JC094iC07p09686.

——, T. B. Sanford, and D. P. Winkel, 2003: Reduced mixing from the breaking of internal waves in equatorial waters. *Nature,* **422,** 513–515, doi:10.1038/nature01507.

Harrison, M., and R. Hallberg, 2008: Pacific subtropical cell response to reduced equatorial dissipation. *J. Phys. Oceanogr.,* **38,** 1894–1912, doi:10.1175/2008JPO3708.1.

Henyey, F. S., J. Wright, and S. M. Flatte, 1986: Energy and action flow through the internal wave field: An Eikonal approach. *J. Geophys. Res.,* **91,** 8487–8495, doi:10.1029/JC091iC07p08487.

Huang, R. X., 1999: Mixing and energetics of the thermocline circulation. *J. Phys. Oceanogr.,* **29,** 727–746, doi:10.1175/1520-0485(1999)029<0727:MAEOTO>2.0.CO;2.

Jing, Z., and L. Wu, 2010: Seasonal variation of turbulent diapycnal mixing in the northwestern Pacific stirred by wind stress. *Geophys. Res. Lett.,* **37,** L23604, doi:10.1029/2010GL045418.

——, and ——, 2013: Low-frequency modulation of turbulent diapycnal mixing by anticyclonic eddies inferred from the HOT time series. *J. Phys. Oceanogr.,* **43,** 824–835, doi:10.1175/JPO-D-11-0150.1.

Kunze, E., 1985: Near-inertial wave-propagation in geostrophic shear. *J. Phys. Oceanogr.,* **15,** 544–565, doi:10.1175/1520-0485(1985)015<0544:NIWPIG>2.0.CO;2.

——, E. Firing, J. M. Hummon, T. K. Chereskin, and A. M. Thurnherr, 2006: Global abyssal mixing inferred from lowered ADCP shear and CTD strain profiles. *J. Phys. Oceanogr.,* **36,** 2350–2352, doi:10.1175/JPO3092.1.

Langlais, C., S. Rintoul, and A. Schiller, 2011: Variability and mesoscale activity of the Southern Ocean fronts: Identification of a circumpolar coordinate system. *Ocean Modell.,* **39,** 79–96, doi:10.1016/j.ocemod.2011.04.010.

Leaman, K. D., and T. B. Sanford, 1975: Vertical energy propagation of internal waves: A vector spectral analysis of velocity profiles. *J. Geophys. Res.,* **80,** 1975–1978, doi:10.1029/JC080i015p01975.

Ledwell, J. R., A. J. Watson, and C. S. Law, 1993: Evidence for slow mixing across the pycnocline from an open-ocean tracer-release experiment. *Nature,* **364,** 701–703, doi:10.1038/364701a0.

——, ——, and ——, 1998: Mixing of a tracer in the pycnocline. *J. Geophys. Res.,* **103,** 21 499–21 529, doi:10.1029/98JC01738.

——, E. T. Montgomery, K. L. Polzin, L. C. St Laurent, R. W. Schmitt, and J. M. Toole, 2000: Evidence for enhanced mixing over rough topography in the abyssal ocean. *Nature,* **403,** 179–182, doi:10.1038/35003164.

Lee, D.-K., and P. P. Niiler, 1998: The inertial chimney: The near-inertial energy drainage from the ocean surface to the deep layer. *J. Geophys. Res.,* **103,** 7579–7591, doi:10.1029/97JC03200.

Levitus, S., and T. P. Boyer, 1994: *Temperature.* Vol. 4, *World Ocean Atlas 1994,* NOAA Atlas NESDIS 4, 117 pp.

Lvov, Y., K. Polzin, and E. Tabak, 2004: Energy spectra of the ocean's internal wave field: Theory and observations. *Phys. Rev. Lett.,* **92,** 128501, doi:10.1103/PhysRevLett.92.128501.

MacKinnon, J. A., M. H. Alford, R. Pinkel, J. M. Klymak, and Z. Zhao, 2013: The latitudinal dependence of shear and mixing in the Pacific transiting the critical latitude for PSI. *J. Phys. Oceanogr.,* **43,** 3–16, doi:10.1175/JPO-D-11-0107.1.

Mauritzen, C., K. L. Polzin, M. S. McCartney, R. C. Millard, and D. E. West-Mack, 2002: Evidence in hydrography and density fine structure for enhanced vertical mixing over the Mid-Atlantic Ridge in the western Atlantic. *J. Geophys. Res.,* **107,** 3147, doi:10.1029/2001JC001114.

Meijers, A. J. S., N. L. Bindoff, and S. R. Rintoul, 2011: Estimating the four-dimensional structure of the Southern Ocean using satellite altimetry. *J. Atmos. Oceanic Technol.,* **28,** 548–568, doi:10.1175/2010JTECHO790.1.

Meyer, A., H. E. Phillips, B. M. Sloyan, and K. L. Polzin, 2014: Mixing (MX) Oceanographic Toolbox for EM-APEX* float data applying shear-strain parameterization. Institute for Marine and Antarctic Studies Tech. Rep., 69 pp.

Munk, W. H., 1966: Abyssal recipes. *Deep-Sea Res. Oceanogr. Abstr.,* **13,** 707–730, doi:10.1016/0011-7471(66)90602-4.

Naveira Garabato, A. C., 2009: RRS James Cook cruise 29, 01 Nov-22 Dec 2008. SOFine cruise report: Southern Ocean

Finestructure. National Oceanography Centre Southampton Cruise Rep. 35, 216 pp.

——, K. I. C. Oliver, A. J. Watson, and M. J. Messias, 2004a: Turbulent diapycnal mixing in the Nordic Seas. *J. Geophys. Res.,* **109,** C12010, doi:10.1029/2004JC002411.

——, K. L. Polzin, B. A. King, K. J. Heywood, and M. Visbeck, 2004b: Widespread intense turbulent mixing in the Southern Ocean. *Science,* **303,** 210–213, doi:10.1126/science.1090929.

——, D. P. Stevens, A. J. Watson, and W. Roether, 2007: Short-circuiting of the overturning circulation in the Antarctic Circumpolar Current. *Nature,* **447,** 194–197, doi:10.1038/nature05832.

Nikurashin, M., and R. Ferrari, 2010: Radiation and dissipation of internal waves generated by geostrophic motions impinging on small-scale topography: Application to the Southern Ocean. *J. Phys. Oceanogr.,* **40,** 2025–2042, doi:10.1175/2010JPO4315.1.

——, and ——, 2011: Global energy conversion rate from geostrophic flows into internal lee waves in the deep ocean. *Geophys. Res. Lett.,* **38,** L08610, doi:10.1029/2011GL046576.

——, and G. K. Vallis, 2012: A theory of the interhemispheric meridional overturning circulation and associated stratification. *J. Phys. Oceanogr.,* **42,** 1652–1667, doi:10.1175/JPO-D-11-0189.1.

——, and R. Ferrari, 2013: Overturning circulation driven by breaking internal waves in the deep ocean. *Geophys. Res. Lett.,* **40,** 3133–3137, doi:10.1002/grl.50542.

Olbers, D., D. Borowski, C. Völker, and J.-O. Wölff, 2004: The dynamical balance, transport and circulation of the Antarctic Circumpolar Current. *Antarct. Sci.,* **16,** 439–470, doi:10.1017/S0954102004002251.

Orsi, A. H., T. Whitworth, and W. D. Nowlin, 1995: On the meridional extent and fronts of the Antarctic Circumpolar Current. *Deep-Sea Res. I,* **42,** 641–673, doi:10.1016/0967-0637(95)00021-W.

Osborne, A. R., and T. L. Burch, 1980: Internal solitons in the Andaman Sea. *Science,* **208,** 451–460, doi:10.1126/science.208.4443.451.

Park, Y. H., E. Charriaud, and M. Fieux, 1998: Thermohaline structure of the Antarctic surface water winter water in the Indian sector of the Southern Ocean. *J. Mar. Syst.,* **17,** 5–23, doi:10.1016/S0924-7963(98)00026-8.

——, J. L. Fuda, I. Durand, and A. C. N. Garabato, 2008: Internal tides and vertical mixing over the Kerguelen Plateau. *Deep-Sea Res. II,* **55,** 582–593, doi:10.1016/j.dsr2.2007.12.027.

Phillips, H. E., and N. L. Bindoff, 2014: On the non-equivalent barotropic structure of the Antarctic Circumpolar Current: An observational perspective. *J. Geophys. Res. Oceans,* **119,** 5221–5243, doi:10.1002/2013JC009516.

Plueddemann, A. J., and J. T. Farrar, 2006: Observations and models of the energy flux from the wind to mixed-layer inertial currents. *Deep-Sea Res. II,* **53,** 5–30, doi:10.1016/j.dsr2.2005.10.017.

Pollard, R. T., and R. C. Millard Jr., 1970: Comparison between observed and simulated wind-generated inertial oscillations. *Deep-Sea Res. Oceanogr. Abstr.,* **17,** 813–821, doi:10.1016/0011-7471(70)90043-4.

Polzin, K. L., J. M. Toole, and R. W. Schmitt, 1995: Finescale parameterizations of turbulent dissipation. *J. Phys. Oceanogr.,* **25,** 306–328, doi:10.1175/1520-0485(1995)025<0306:FPOTD>2.0.CO;2.

——, K. G. Speer, J. M. Toole, and R. W. Schmitt, 1996: Intense mixing of Antarctic Bottom Water in the equatorial Atlantic Ocean. *Nature,* **380,** 54–57, doi:10.1038/380054a0.

——, J. M. Toole, J. R. Ledwell, and R. W. Schmitt, 1997: Spatial variability of turbulent mixing in the abyssal ocean. *Science,* **276,** 93–96, doi:10.1126/science.276.5309.93.

Polzin, K., E. Kunze, J. Hummon, and E. Firing, 2002: The finescale response of lowered ADCP velocity profiles. *J. Atmos. Oceanic Technol.,* **19,** 205–224, doi:10.1175/1520-0426(2002)019<0205:TFROLA>2.0.CO;2.

——, ——, J. M. Toole, and R. W. Schmitt, 2003: The partition of finescale energy into internal waves and subinertial motions. *J. Phys. Oceanogr.,* **33,** 234–248, doi:10.1175/1520-0485(2003)033<0234:TPOFEI>2.0.CO;2.

——, A. C. Naveira Garabato, T. N. Huussen, B. M. Sloyan, and S. N. Waterman, 2014: Finescale parameterizations of turbulent dissipation. *J. Geophys. Res. Oceans,* **119,** 1383–1419, doi:10.1002/2013JC008979.

Rintoul, S. R., and A. C. Naveira Garabato, 2013: Dynamics of the Southern Ocean circulation. *Ocean Circulation and Climate: A 21st Century Perspective,* 2nd ed., G. Siedler et al., Eds., International Geophysics Series, Vol. 103, Elsevier, 471–492.

Sallée, J. B., K. Speer, and R. Morrow, 2008: Response of the Antarctic Circumpolar Current to atmospheric variability. *J. Climate,* **21,** 3020–3039, doi:10.1175/2007JCLI1702.1.

Sanford, T. B., R. G. Drever, and J. H. Dunlap, 1978: A velocity profiler based on the principles of geomagnetic induction. *Deep-Sea Res.,* **25,** 183–210, doi:10.1016/0146-6291(78)90006-1.

Sloyan, B. M., 2005: Spatial variability of mixing in the Southern Ocean. *Geophys. Res. Lett.,* **32,** L18603, doi:10.1029/2005GL023568.

——, and S. R. Rintoul, 2001: The Southern Ocean limb of the global deep overturning circulation. *J. Phys. Oceanogr.,* **31,** 143–173, doi:10.1175/1520-0485(2001)031<0143:TSOLOT>2.0.CO;2.

——, L. D. Talley, T. K. Chereskin, R. Fine, and J. Holte, 2010: Antarctic Intermediate Water and Subantarctic Mode Water formation in the southeast Pacific: The role of turbulent mixing. *J. Phys. Oceanogr.,* **40,** 1558–1574, doi:10.1175/2010JPO4114.1.

Smith, W. H. F., and D. T. Sandwell, 1997: Global sea floor topography from satellite altimetry and ship depth soundings. *Science,* **277,** 1956–1962, doi:10.1126/science.277.5334.1956.

Sokolov, S., and S. R. Rintoul, 2007: Multiple jets of the Antarctic Circumpolar Current south of Australia. *J. Phys. Oceanogr.,* **37,** 1394–1412, doi:10.1175/JPO3111.1.

——, and ——, 2009: Circumpolar structure and distribution of the Antarctic Circumpolar Current fronts: 1. Mean circumpolar paths. *J. Geophys. Res.,* **114,** C11018, doi:10.1029/2008JC005108.

St. Laurent, L. C., J. M. Toole, and R. W. Schmitt, 2001: Buoyancy forcing by turbulence above rough topography in the abyssal Brazil basin. *J. Phys. Oceanogr.,* **31,** 3476–3495, doi:10.1175/1520-0485(2001)031<3476:BFBTAR>2.0.CO;2.

——, A. C. Naveira Garabato, J. R. Ledwell, A. M. Thurnherr, J. M. Toole, and A. J. Watson, 2012: Turbulence and diapycnal mixing in Drake Passage. *J. Phys. Oceanogr.,* **42,** 2143–2152, doi:10.1175/JPO-D-12-027.1.

Thompson, A. F., S. T. Gille, J. A. MacKinnon, and J. Sprintall, 2007: Spatial and temporal patterns of small-scale mixing in Drake Passage. *J. Phys. Oceanogr.,* **37,** 572–592, doi:10.1175/JPO3021.1.

Thorpe, S. A., 2005: *The Turbulent Ocean.* Cambridge University Press, 439 pp.

Toggweiler, J. R., and B. Samuels, 1995: Effect of Drake Passage on the global thermohaline circulation. *Deep-Sea Res. I,* **42,** 477–500, doi:10.1016/0967-0637(95)00012-U.

——, and ——, 1998: On the ocean's large-scale circulation near the limit of no vertical mixing. *J. Phys. Oceanogr.,* **28,** 1832–1852, doi:10.1175/1520-0485(1998)028<1832:OTOSLS>2.0.CO;2.

van Meurs, P., 1998: Interactions between near-inertial mixed layer currents and the mesoscale: The importance of spatial

variabilities in the vorticity field. *J. Phys. Oceanogr.,* **28,** 1363–1388, doi:10.1175/1520-0485(1998)028<1363:IBNIML>2.0.CO;2.

Walin, G., 1982: On the relation between sea-surface heat flow and thermal circulation in the ocean. *Tellus,* **34,** 187–195, doi:10.1111/j.2153-3490.1982.tb01806.x.

Watanabe, M., and T. Hibiya, 2002: Global estimates of the wind-induced energy flux to inertial motions in the surface mixed layer. *Geophys. Res. Lett.,* **29,** 1239, doi:10.1029/2001GL014422.

Waterhouse, A. F., and Coauthors, 2014: Global patterns of diapycnal mixing from measurements of the turbulent dissipation rate. *J. Phys. Oceanogr.,* **44,** 1854–1872, doi:10.1175/JPO-D-13-0104.1.

Waterman, S., A. C. Naveira Garabato, and K. L. Polzin, 2013: Internal waves and turbulence in the Antarctic Circumpolar Current. *J. Phys. Oceanogr.,* **43,** 259–282, doi:10.1175/JPO-D-11-0194.1.

——, K. L. Polzin, A. C. Naveira Garabato, K. L. Sheen, and A. Forryan, 2014: Suppression of internal wave breaking in the Antarctic Circumpolar Current near topography. *J. Phys. Oceanogr.,* **44,** 1466–1492, doi:10.1175/JPO-D-12-0154.1.

Whalen, C. B., L. D. Talley, and J. A. MacKinnon, 2012: Spatial and temporal variability of global ocean mixing inferred from Argo profiles. *Geophys. Res. Lett.,* **39,** L18612, doi:10.1029/2012GL053196.

Whitworth, T., and W. D. Nowlin, 1987: Water masses and currents of the Southern Ocean at the Greenwich meridian. *J. Geophys. Res.,* **92,** 6462–6476, doi:10.1029/JC092iC06p06462.

Winters, K. B., and E. A. D'Asaro, 1997: Direct simulation of internal wave energy transfer. *J. Phys. Oceanogr.,* **27,** 1937–1945, doi:10.1175/1520-0485(1997)027<1937:DSOIWE>2.0.CO;2.

Wu, L., Z. Jing, S. Riser, and M. Visbeck, 2011: Seasonal and spatial variations of Southern Ocean diapycnal mixing from Argo profiling floats. *Nat. Geosci.,* **4,** 363–366, doi:10.1038/ngeo1156.

Wunsch, C., 1998: The work done by the wind on the oceanic general circulation. *J. Phys. Oceanogr.,* **28,** 2332–2340, doi:10.1175/1520-0485(1998)028<2332:TWDBTW>2.0.CO;2.

——, and R. Ferrari, 2004: Vertical mixing, energy and the general circulation of the oceans. *Annu. Rev. Fluid Mech.,* **36,** 281–314, doi:10.1146/annurev.fluid.36.050802.122121.